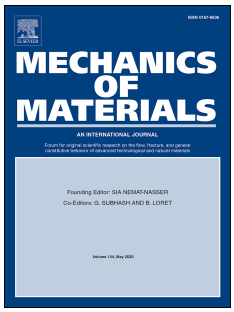

Unravelling the effects of ratcheting and constraint on the cyclic behaviour of a martensitic steel under elevated temperature

Raheeg Ragab, Yong Pang, Tao Liu, Nigel Neate, Ming Li, Wei Sun

PII: S0167-6636(23)00154-0

DOI: https://doi.org/10.1016/j.mechmat.2023.104708

Reference: MECMAT 104708

To appear in: *Mechanics of Materials*

Received Date: 24 January 2023

Revised Date: 19 May 2023

Accepted Date: 30 May 2023

Please cite this article as: Ragab, R., Pang, Y., Liu, T., Neate, N., Li, M., Sun, W., Unravelling the effects of ratcheting and constraint on the cyclic behaviour of a martensitic steel under elevated temperature, *Mechanics of Materials* (2023), doi: https://doi.org/10.1016/j.mechmat.2023.104708.

CRediT authorship contribution statement

Raheeg Ragab: Conceptualization, Methodology, Software, Formal analysis, Investigation, Data curation, Writing – original draft. **Yong Pang**: Methodology, Writing – review & editing. **Tao Liu:** Methodology, Writing – review & editing, Supervision, Project administration, Funding acquisition. **Nigel Neate**: TEM Characterisation, Writing – review & editing. **Ming Li:** Supervision, Methodology. **Wei Sun:** Conceptualization, Methodology, Writing – review & editing, Supervision, Project administration, Funding acquisition.

Unravelling the Effects of Ratcheting and Constraint on the Cyclic Behaviour of a Martensitic Steel under Elevated Temperature

Raheeg Ragab[1*], Yong Pang[2], Tao Liu[2**], Nigel Neate[3], Ming Li[4***], Wei Sun[1]

[1]Faculty of Engineering, University of Nottingham, Nottingham NG7 2RD, UK

[2]School of Engineering and Materials Science, Queen Mary University of London

[3] Nanoscale and Microscale Research Centre, University of Nottingham, Nottingham NG7 2RD, UK

[4]School of Mechanics, Civil Engineering and Architecture, Northwestern Polytechnical University, Xi'an 710072, China

ABSTRACT

This work examines important aspects of the high-temperature cyclic visco-plasticity behaviour, namely the ratcheting (cyclic creep) and constraint effects, under low-cycle fatigue (LCF) via experimental characterisation and physically based damage modelling. For this purpose, fully-reversed, load-controlled uniaxial and multi-axial saw-tooth (SWT) low cycle fatigue tests were carried out on a martensitic steel (FV566) at 600^{o}C Further, an improved physically-based viscoplasticity modelling framework is introduced, which links the material microstructural properties to the constitutive mechanical behaviour, thereby allowing us to explore the ratcheting and constraint effects not only at the macro level but also at the subgrain level. The Finite Element (FE) analyses were complemented by detailed microstructural characterisation of the tested samples to unveil the key mechanisms contributing to the cyclic visco-plasticity damage in the FV566 steel at high temperatures. Based on this investigation, the micromechanics origin of the softening was elucidated. Moreover, the micro-damage modelling results in conjunction with the physical characterisation offered an improved mechanistic understanding of fatigue notch strengthening behaviour in multi-axial LCF tests. Importantly, an additional cyclic degradation mechanism was captured in the presence of constraints, which relates to the precipitate coarsening behaviour.

Keywords: *Visco-plasticity; Cyclic softening; Micro-damage; Ratcheting; Constraint; Notch strengthening*

*Corresponding author Raheeg.ragab@nottingham.ac.uk (R. Ragab)

**Corresponding author tao.liu@qmul.ac.uk (T. Liu)

***Corresponding author ming.li1@nwpu.edu.cn (M. Li)

1. INTRODUCTION

FV566 (X12CrNiMoVNb) is a novel martensitic steel candidate commonly adopted as a high-temperature material for gas turbine components owing to its superior high-temperature mechanical properties and improved oxidation resistance [1, 2]. Such attractive features are derived from the microstructure of the FV566 steel, which exhibits hierarchical arrangements consisting of prior austenite grains, packets, blocks and martensitic laths [3-5].

Due to the requirement for modern powerplants to operate under flexible operation mode to match the increasing energy demand whilst maintaining reduced carbon emissions, these materials are now subjected to ever-increasing temperature and pressure conditions. Such extreme conditions can result in severe creep, fatigue and creep-fatigue damage, which may potentially limit the service life of energy components. This has recently attracted some research to further explore the important aspects of cyclic deformation and damage behaviour of 9-12%Cr martensitic steel, with the strain-controlled tests being commonly investigated [1,2, 5-10]. Based on previous work, it was shown that materials under strain-controlled LCF could experience cyclic softening accompanied by various microstructural changes such as annihilation of mobile dislocation and martensite lath instability [2, 11-14]. Nonetheless, cyclic softening can also occur under stress-controlled cycling [15-19], and this is typically manifested by the presence of the ratcheting (cyclic creep), which induces an accumulation of the visco-plastic strain with the increasing number of cycles, posing serious consequences on the structural integrity of engineering structures at high temperatures. Therefore, an in-depth understanding of the cyclic response and the associated damage mechanisms of high-temperature materials such as FV566 steels under stress-controlled low-cycle fatigue becomes of great scientific and technological interest.

Since engineering structures typically operate under multi-axial stress states (due to the presence of geometrical and/or material discontinuities), the effect of constraints on the LCF performance at elevated temperatures becomes another important aspect to examine [20]. In the literature, however, numerous studies have focused primarily on the multi-axial creep behaviour using experimental notched bar rupture tests (e.g., refs [21-24]). For instance, notched bar creep tests with different notch geometries were conducted, followed by fractography examinations of the tested samples [21, 22]. It was found that the notch constraint can significantly influence the multi-axial creep deformation and fracture mechanisms [21, 22]. Further, depending on the material ductility, stress level and notch geometry, the material can show either notch strengthening or weakening [25]. Whilst these are interesting findings, it is important to extend the scope of the work and examine the cyclic behaviour under constrained conditions, which will be addressed in our current work. Although a few researchers have recently attempted to study the notch effect on the low-cycle fatigue performance numerically and/or experimentally [47, 48], the underlying mechanisms governing the notch (constraint) effect on the cyclic visco-plasticity behaviour remain unclear, which raises the need for more systematic investigations to fully uncover the notch effects and the associated governing mechanisms.

Constitutive material models and theoretical frameworks have been developed to represent the cyclic plasticity behaviour at high temperatures. These can be classified into unified [26-28] and non-unified viscoplasticity models [29]. The former category uses the inelastic strain to represent both the time-dependent creep deformation and rate-independent plasticity [26],

while the latter treats creep and plasticity separately. At elevated temperatures, however, the interaction between creep and plasticity becomes stronger and unified theories are thus favoured in modelling the visco-plastic deformation. Chaboche's visco-plasticity model is commonly adopted among the unified theories to represent the high-temperature cyclic deformation behaviour [26, 30, 31]. The model comprises a visco-plastic flow rule combined with isotropic and kinematic hardening rules [26]. However, a significant limitation of this model is that not all the cyclic softening stages can be successfully captured [10]. To overcome this drawback, additional variables have been incorporated within the unified visco-plasticity framework to capture the damage during cyclic loading [3, 5, 7] in accordance with continuum damage mechanics [32, 33]. Considerable efforts have been devoted towards modelling the cyclic softening of advanced high chromium steels under strain-controlled mode utilising phenomenological and physically based constitutive models (e.g., refs [3, 34-36]). In reality, however, engineering structures can experience both strain and stress-controlled cycling, and therefore, establishing a modelling methodology to simulate the cyclic softening under stress-controlled fatigue becomes vital. Whilst some empirically based approaches were established and showed good potential for the assessment of ratcheting and fatigue failure under load-controlled tests [37-40], it is more desirable to present a physically based damage modelling capability which can link the macroscopic observations of the deformation in advanced materials like FV566 steel to the microstructural evolutions during load-controlled cycling. Therefore, an improved physically based modelling capability is introduced in the current paper, which helps us explore the effects of the ratcheting and constraints not only at the macro-level but also at finer length scales.

In light of these, our current work aims to provide an improved mechanistic understanding of the notch (constraint) and ratcheting effects on the cyclic visco-plasticity behaviour of martensitic steels at elevated temperatures by employing integrated experimental and theoretical approaches. The remainder of this paper is structured as follows: In Section 2, details of the experimental work conducted to characterise the mechanical behaviour of FV566 steel under load-controlled LCF are outlined. Following, the key experimental data obtained from the mechanical tests are presented and analysed in Section 3. Section 4 presents the viscoplastic constitutive material model coupled with an improved physically based damage model, which will be utilized in this work to simulate the cyclic viscoplastic deformation and damage under LCF tests. The key findings from this study are presented and discussed in Section 5. Finally, some concluding remarks and proposals for future work are provided in Section 6.

2. EXPERIMENTAL METHODS

In this Section, we present an outline of the experimental methods employed in this investigation, namely those relating to cyclic mechanical tests (Section 2.1) and microstructural characterisation (Section 2.2).

2.1 Materials and Low Cycle Fatigue Tests

The material used in this work is FV566 martensitic stainless steel which was extracted from a location close to the centreline of a service-aged gas turbine rotor which had operated for about 90,000 hours at a maximum speed of 3000 rpm [1, 2]. The chemical composition of the material is listed in Table (1). The microstructural characteristics of this material in the as-received state including grain size and misorientationis have been reported elsewhere [2].

Table (1): Chemical Composition of the FV566 steel (by wt.%)

C	Si	Mn	Cr	Mo	Ni	V	S	Fe
0.6	0.038	0.668	11.9	1.68	2.52	0.298	0.006	remainder

In this work, fully reversed uniaxial and multi-axial load-controlled low cycle fatigue (LCF) tests were conducted at 600^{o}C in the air to characterise the visco-plastic and cyclic softening behaviour of the FV566 steel at different stress states (constraints). To achieve this aim, smooth (unnotched) and notched cylindrical fatigue specimens (with a gauge diameter of 5mm and a gauge length of 10mm) were machined as per the ISO 12106 standard. The smooth round bar used in the uniaxial cyclic test is schematically shown in Fig.1a, while the notched bar used in the multi-axial cyclic test is shown in Fig.1b. The introduction of notch imposes local constraints on deformation and thereby results in a multi axial stress state. Symmetrical saw-tooth triangular loading waveform (SWT) without hold periods (shown in Fig.1c) was applied at a constant axial force amplitude, resulting in a nominal stress rate of approximately 1.9 MPa/s. The cyclic test conditions (temperature and loading) were selected to give a representative behaviour to that experienced by a typical gas turbine component in service. The uniaxial and notched bar cyclic tests were conducted under push-pull cyclic loading with nominal stress control using a closed-loop servo-hydraulic testing machine equipped with a high-temperature furnace. The loading ratio was maintained at -1 during the cyclic tests. The temperature along the gauge length was controlled during the tests using thermocouples attached to the specimen. The main experimental outputs from these experiments are the hysteresis response of the material and the cyclic softening (ratcheting deformation). A summary of the key results obtained from the uniaxial and notched bar cyclic tests are provided in Section 3.

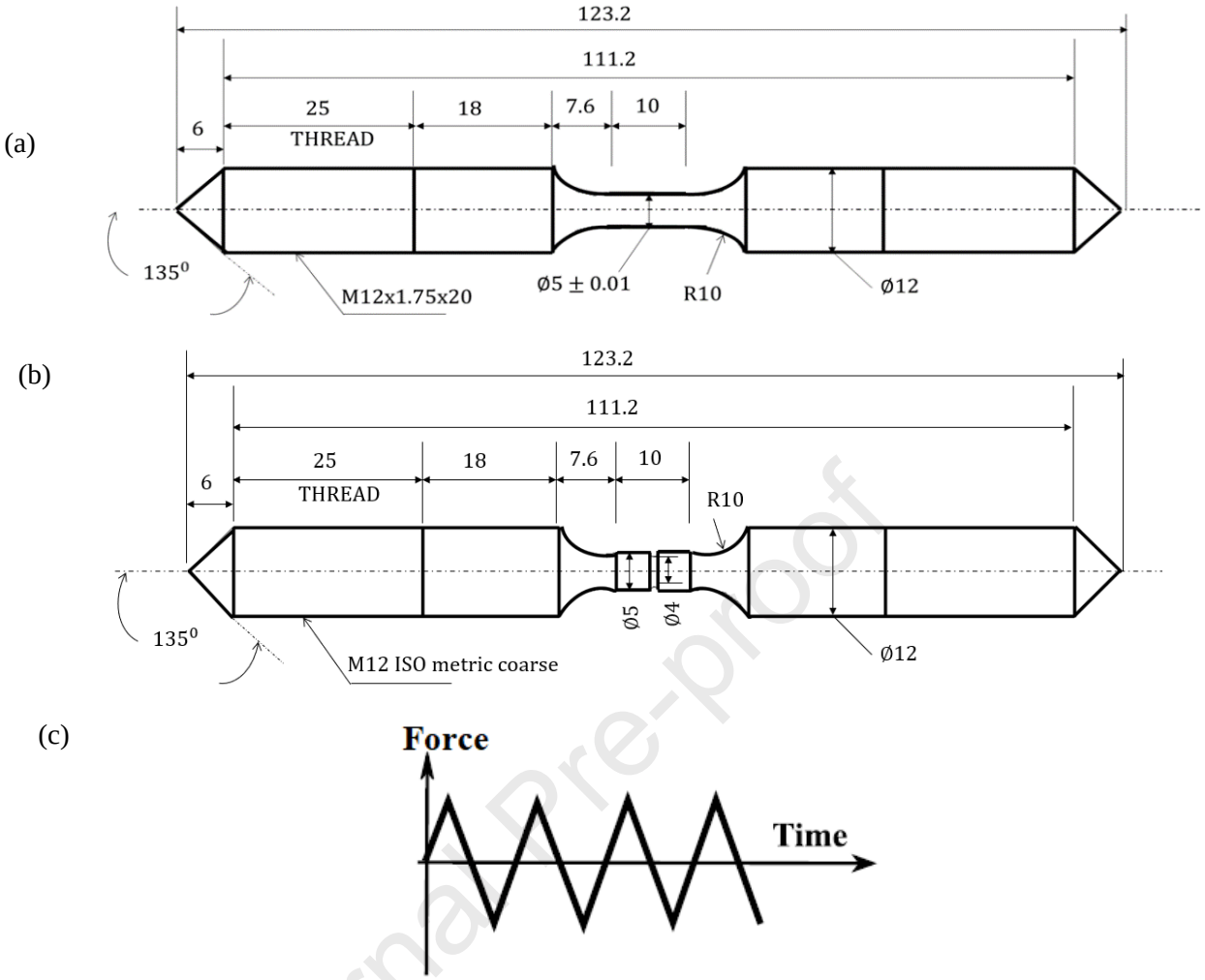

Fig.1: Details and dimensions of the round bar specimens used in the load-controlled LCF tests as well as the load waveform. a) Uniaxial plain bar specimen, b) Notched bar specimen, and c) Triangular load waveform employed in the cyclic mechanical test.

2.2 Microstructure Characterisation

The cyclic mechanical tests (outlined in Section 2.1) were complemented by microstructural examinations of the tested FV566 steels to characterise the softening mechanisms and the fracture behaviour due to stress cycling. In this way, the macroscopic observations can be related to the evolution of microstructural features. We employed a variety of analytical techniques such as Scanning Electron Microscopy (SEM), Energy-dispersive X-ray spectroscopy (EDS) and Transmission Electron Microscopy (TEM) as further elaborated below.

2.2.1 SEM and EDS Analyses

Fractographic inspections were conducted on the fracture surface of the uniaxial plain bar and notched bar specimens. Ruptured surfaces were sectioned from these specimens using electrical discharge machining, cleaned by an ultrasonic cleaner, and mounted on specimen stubs for SEM imaging. A JEOL JSM-7000F field-emission SEM was employed to characterise fracture surfaces at a working distance of approximately 25 mm and an accelerating voltage of 15 kV. EDS analysis was conducted using Oxford instruments AZtec

software to confirm the chemical compositions of inclusions on fracture surfaces. An accelerating voltage of 20 kV was used in the EDS analysis.

2.2.2 TEM Analysis

In the present study, Transmission Electron Microscopy (TEM) was conducted to investigate the microstructure recovery at the micron and submicron levels due to LCF. Lamellae, which are very thin samples, were prepared for TEM from the bulk material by sectioning, deposition and thinning using a FEI Quanta 200 3D focused ion beam (FIB) SEM system. The lamellae were further thinned to approximately 100 nm using a Zeiss Crossbeam 550 FIB-SEM, with final ion beam polishing at 5 kV to minimise damage. Bright-field images were then acquired in two-beam conditions (where the dominant contrast mechanism is diffraction) to enable capturing of the dislocations and other crystal defects using a JEOL JEM-2100Plus TEM with an accelerating voltage of 200 kV.

3. EXPERIMENTAL RESULTS

In this Section, the experimental data acquired from the uniaxial and multi-axial low-cycle fatigue tests are analysed to explore the range of parameters influencing the cyclic deformation and damage behaviour in FV566 steels such as the load level and stress state (constraint).

3.1 Fatigue Life

The experimental fatigue lives of the FV566 steel tested under uniaxial and multi-axial load-controlled cyclic conditions are illustrated in Table (2). Fatigue life shortens as the applied load increases from 7360N to 8060N. Notch-strengthening behaviour can be observed for this material under the given testing conditions (that is fatigue life improves with the introduction of notches). Some possible interpretations of this behaviour are presented later in the paper with the aid of the micro-damage modelling and physical characterisation of the tested samples. The notch strengthening factor (ratio of notched bar fatigue life to that of the plain bar at the same test conditions) appears to increase with increasing load magnitude.

Table (2): A summary of the experimentally measured fatigue lives of the FV566 uniaxial and notched bars at 600^{o}C under load-controlled LCF

Temp. ^{o}C	Axial force amplitude (N)	Notched bar fatigue life (cycles)	Plain bar fatigue life (cycles)
600	7360	358	194
600	8060	215	60

3.2 Hysteresis Response and Cyclic Strain Ratio

The experimentally measured hysteresis responses of the FV566 steel at different fatigue life stages and under uniaxial cyclic conditions are shown in terms of the engineering stress versus engineering strain, as illustrated in Fig.2. For the given cyclic mechanical testing conditions, a progressive translation of the hysteresis loops can be observed during repeated load cycles,

indicating softening. The peak tensile strain recorded at a given fatigue life ratio increases as the applied axial force increases from 7360N to 8060N.

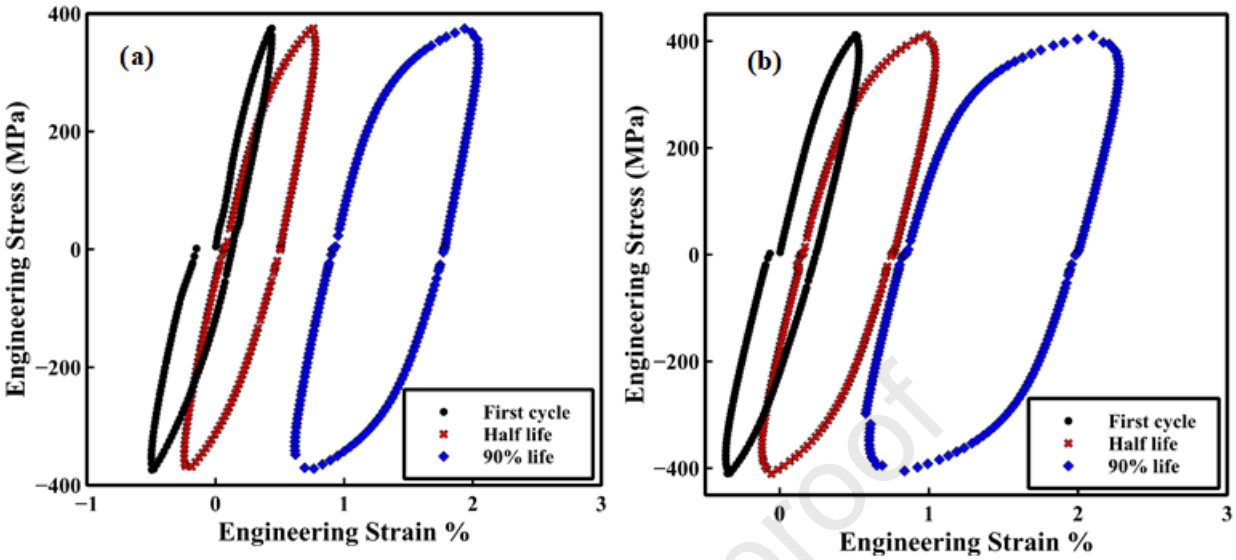

Fig.2: The hysteresis response of the FV566 'plain bar' at 600°C under uniaxial load-controlled LCF tests subjected to axial forces of a) 7360N, b) 8060N.

To gain further insights into the evolution of elastic and inelastic strains during cycles, the cyclic strain ratio (CSR) is determined based on the hysteresis response of the material as follows:

$$CSR = \frac{\Delta\varepsilon_p}{\Delta\varepsilon_e} \tag{1}$$

where $\Delta\varepsilon_p$ and $\Delta\varepsilon_e$ are the plastic strain range and elastic strain range, respectively.

Figure 3 shows the evolution of CSR. Here, the number of cycles (N) is normalised with respect to fatigue failure life (N_f). It can be observed that the inelastic strain increases continuously for a given load magnitude as the number of cycles evolves. Further, the fatigue life stage where the proportion of the cyclic plastic strain surpasses that of the elastic strain (i.e., when the cyclic strain ratio > 1) can be identified, as illustrated in Fig.3.

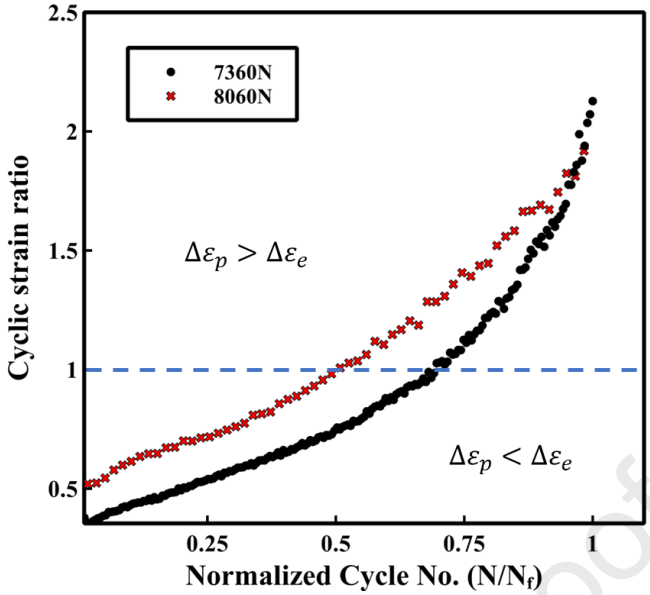

Fig.3: Evolution of cyclic strain ratio with cycles for the FV566 'plain bar' under uniaxial load-controlled LCF tests at 600°C.

3.3 Cyclic Softening and Ratcheting

The FV566 material exhibits cyclic softening under the fully reversed load-controlled tests, as shown in Fig.4a and Fig.4b. A progressive increase in the axial strain with cycles can be observed, known as ratcheting. In Fig.4a and Fig.4b, the ratcheting strain during different fatigue live stages is measured as the mean value of the peak strain (ε_{max}) and minimum strain (ε_{min}) recorded for each cycle, as defined below:

$$\varepsilon_r = \frac{\varepsilon_{max} + \varepsilon_{min}}{2} \tag{2}$$

For the different loading conditions, it can be seen that during the early fatigue life stages, the reversibility of the plastic deformations is almost maintained, resulting in minor ratcheting. Beyond this ratio, the ratcheting becomes more significant, possibly due to the tension-compression asymmetry behaviour observed, which implies that the resistance of the material to strain accumulation in tension is different than in compression [41, 42]. Overall, the ratcheting strain (mean strain) accumulates in the tension direction throughout the different fatigue life stages. As shown in Fig.4c, the ratcheting accumulates in three typical stages, which can be classified into stage I, with a decreasing ratcheting rate; stage II, with a constant ratcheting rate; and stage III, where ratcheting accumulates more rapidly. The ratcheting rate increases with the load magnitude, as shown in Fig.4c.

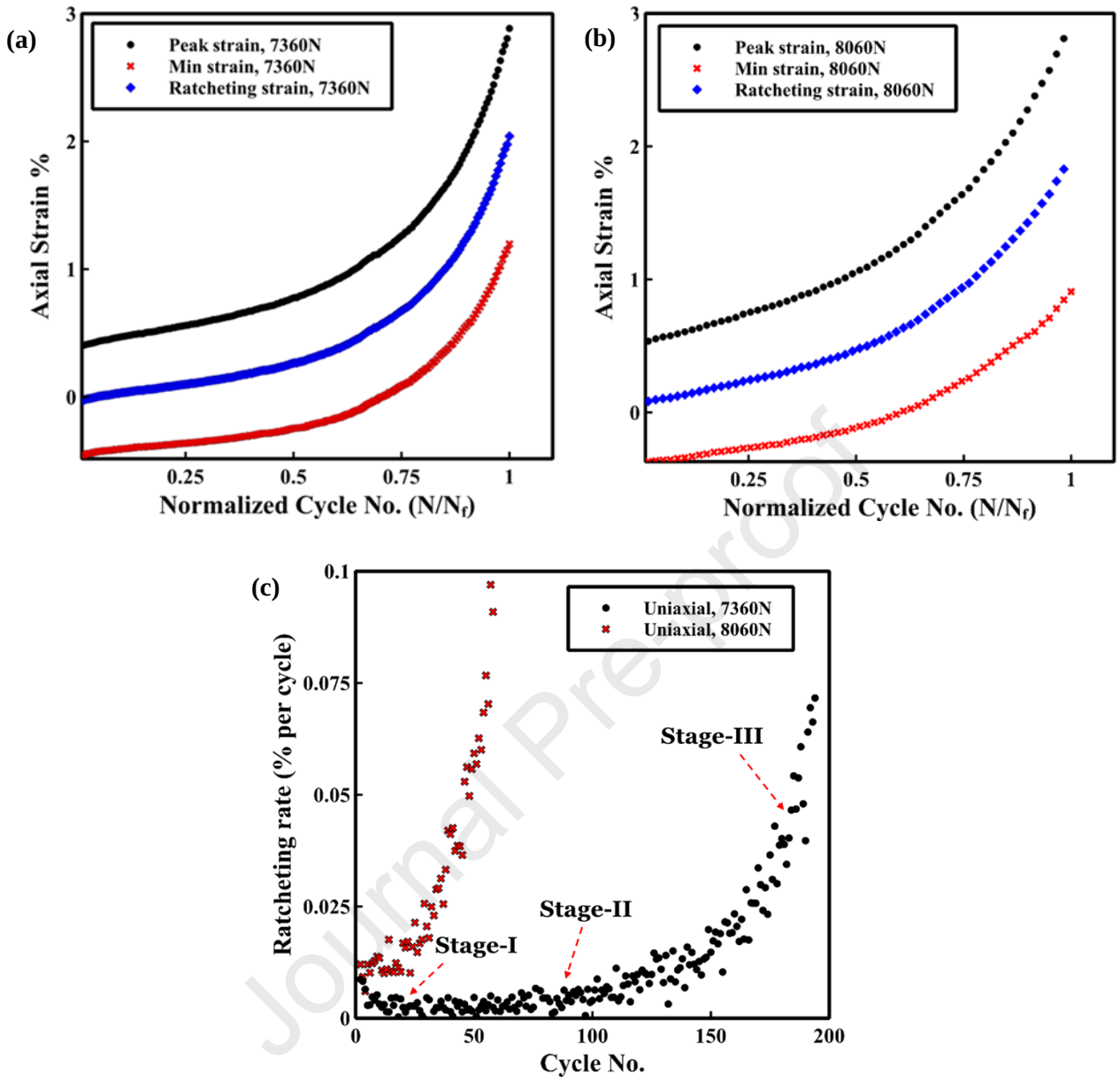

Fig.4: Evolution of peak strain, minimum strain and ratcheting strain with cycles for the FV566 'plain bar' at 600°C under uniaxial load-controlled cyclic conditions of a) 7360N, and b) 8060N. c) Variation of the measured ratcheting rates $\left(\frac{d\varepsilon_r}{dN}\right)$ for the FV566 steel at 600°C under different uniaxial LCF conditions.

An alternative measure of cyclic softening under load-controlled LCF tests is the strain range evolution (Fig.5) which is analogous to the stress range vs cycles ($\Delta\sigma - N$) curve for strain-controlled LCF tests. The strain range is calculated as the difference between the peak strain and minimum strain ($\Delta\varepsilon = \varepsilon_{max} - \varepsilon_{min}$). A monotonically increasing strain range with cycles can be observed, indicating strain softening behaviour. The corresponding stress-strain responses at various fatigue life fractions are also presented, which reveal the expansion of the hysteresis loops due to cyclic plasticity damage under stress-controlled LCF.

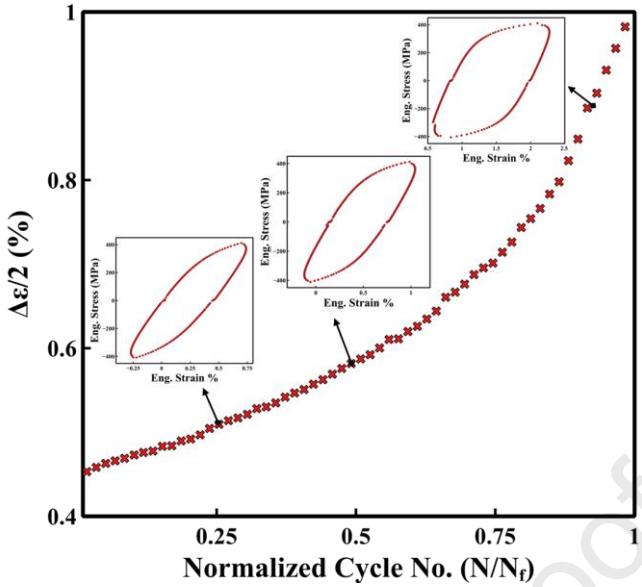

Fig.5: Strain range evolution for the FV566 'plain bar' under uniaxial load-controlled LCF (axial force 8060N, temperature 600^{o}C).

Under a multi-axial stress state, similar deformation behaviour can be noted where the axial strain accumulates with increasing cycles, as depicted in Fig.6. However, the multi-axial ratcheting measured at a particular load level appears to be less significant than the uniaxial ratcheting at the same cyclic conditions, as shown in Fig.7a. Similar observations were noted by [41- 43]. In addition, comparing the nominal stress-strain response of the uniaxial plain bar to that exhibited by the multi-axial notched bar shows more energy dissipation by cycle under uniaxial LCF, indicating more damage (softening) in the material, as can be inferred from the hysteresis loops areas in Fig.7b. Such behaviour can partially explain the beneficial effect of the notch constraint on fatigue life (i.e., notch strengthening), as demonstrated in Table (2). Some mechanistic insights into the effects of notch constraint on the cyclic viscoplasticity damage behaviour are outlined in Section 5.

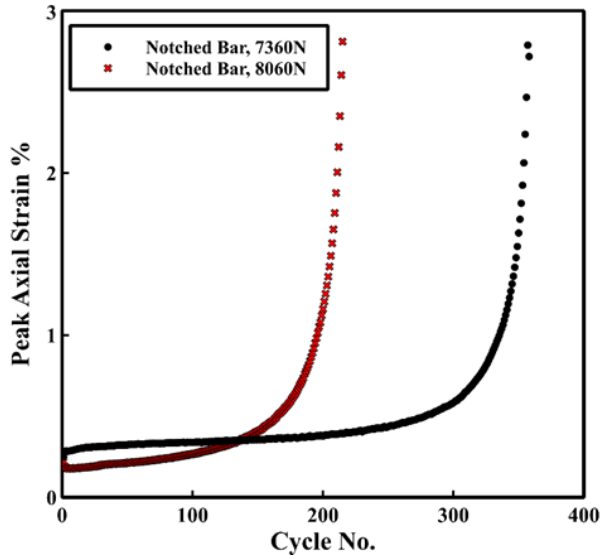

Fig.6: Comparison of the experimentally measured peak axial strain evolution in the multi-axial notched bar LCF tests under different axial forces at 600^{o}C.

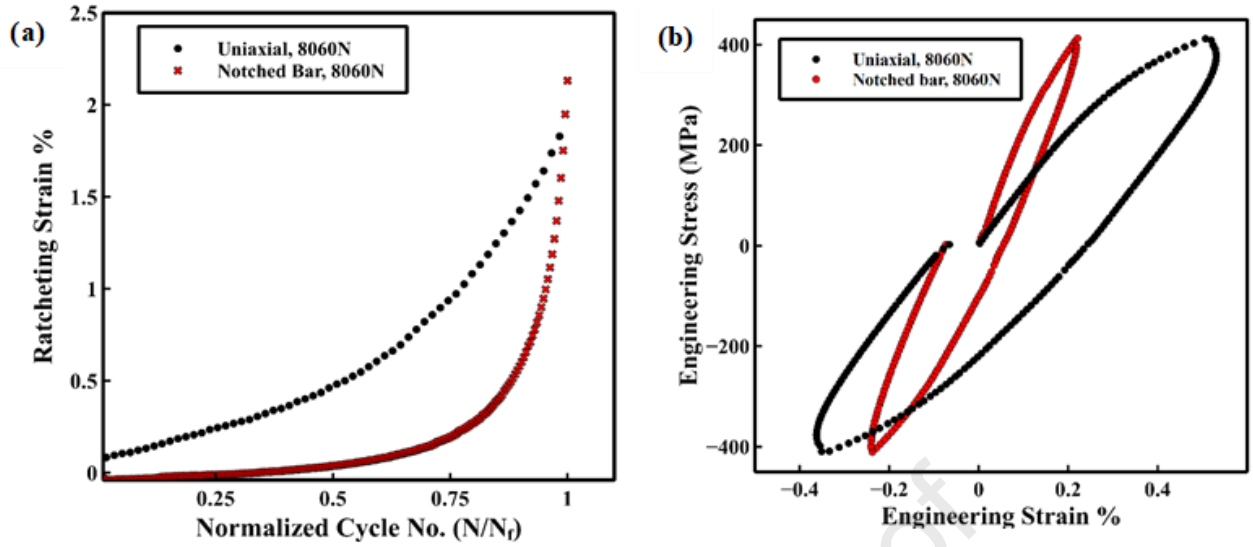

Fig.7: Comparison of the multi-axial and uniaxial LCF response of the FV566 steel (under an axial force amplitude of 8060N at 600^{o}C), showing a) Ratcheting behaviour, and b) Nominal stress vs Nominal axial strain.

3.4 Role of Back Stress on Cyclic Softening

The back stress corresponds to the long-range interaction of dislocations with obstacles such as grain and subgrain boundaries [19, 45]. In stress space, the back stress can be identified as the shift in the centre of the yield surface, as shown in Fig.8a. To quantify the contribution of the back stress component to cyclic softening, its evolution under uniaxial LCF conditions was determined from the hysteresis loops, utilising the Cottrell's stress partition method [46]. As illustrated in Fig.8b, the back stress continuously reduces during loading cycles and three stages of softening can be identified. The first stage is characterised by rapid softening, while the second stage presents a stable softening. Finally, an accelerated reduction in back stress can be observed in the last stage before failure. Overall, the ratcheting deformation developed under stress cycling is driven by the decay of the back stress. The underlying physical mechanisms contributing to back stress softening are discussed in Section 5.2.

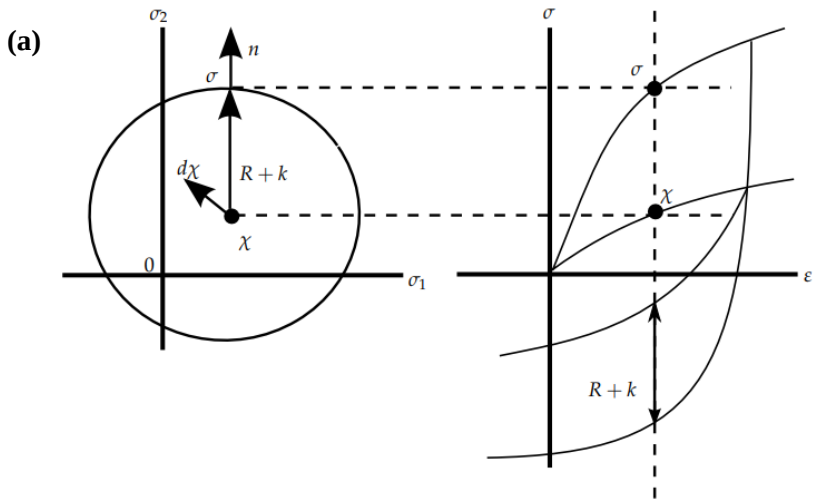

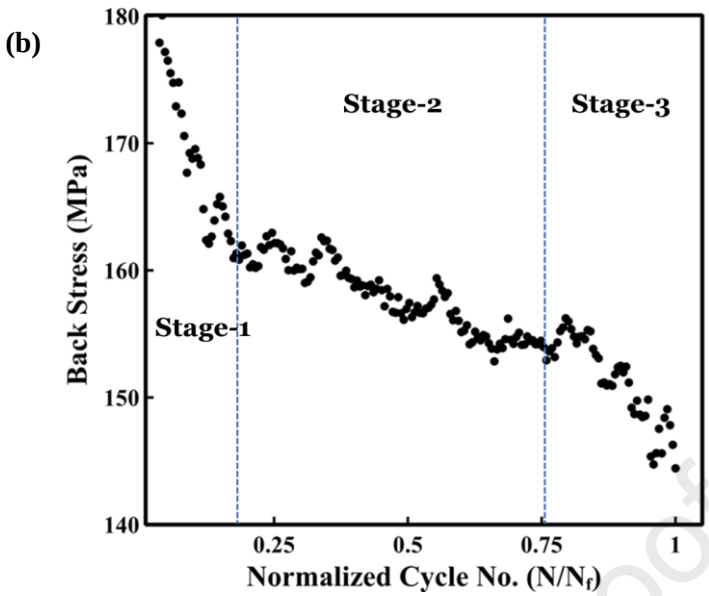

Fig.8: a) A schematic diagram outlining how the back stress is determined from the hysteresis loop based on Cottrell's stress partition method [46]; b) Evolution of back stress with cycles for the FV566 plain bar at 600^{o}C under uniaxial load-controlled LCF of 7360N.

4. THEORITICAL FRAMEWORK

This Section presents a damage-coupled visco-plastic constitutive model, which will be implemented to simulate the material cyclic deformation and damage behaviour. The unified visco-plasticity (UVP) framework is presented in Section 4.1, while an improved physically based damage model is introduced in Section 4.2.

4.1 Unified Viscoplastic Constitutive Model

Within the unified visco-plasticity framework, the total strain tensor, $\boldsymbol{\varepsilon_{ij}^{t}}$, can be decomposed into elastic, $\boldsymbol{\varepsilon_{ij}^{e}}$, and viscoplastic $\boldsymbol{\varepsilon_{ij}^{vp}}$, parts as given below (assuming small deformations):

$$\boldsymbol{\varepsilon_{ij}^{t}} = \boldsymbol{\varepsilon_{ij}^{e}} + \boldsymbol{\varepsilon_{ij}^{vp}} \tag{3}$$

Assuming isotropic damage, Hooke's law of elasticity coupled with the damage variable, $D \in [0,1]$, can be expressed as [33]:

$$\boldsymbol{\varepsilon_{ij}^{e}} = \left(\frac{1+\nu}{E}\,\frac{\boldsymbol{\sigma_{ij}}}{1-D}\right) - \frac{\nu}{E\,(1-D)}\,tr(\boldsymbol{\sigma})\,I \tag{4}$$

$$\boldsymbol{\sigma_{ij}} = \boldsymbol{C}\colon\left(\boldsymbol{\varepsilon_{ij}^{t}} - \boldsymbol{\varepsilon_{ij}^{vp}}\right) \tag{5}$$

where ν, E are the Poisson's ratio and Young's modulus, respectively; $\boldsymbol{\sigma_{ij}}$ and $tr(\boldsymbol{\sigma})$ are the stress tensor and the trace of the stress tensor, respectively; I is the unit tensor of the second-rank; $\boldsymbol{C}$ is the fourth-order elastic stiffness tensor. The symbol ":" denotes the double-contracted product.

The viscoplastic potential surface can be expressed as follows:

$$\Omega(f) = \frac{Z}{n+1}\left\langle\frac{f}{Z}\right\rangle^{n+1} \tag{6}$$

The viscoplastic flow rule coupled with the isotropic damage can be defined as follows by utilising the normality hypothesis of visco-plasticity (that is the rate of the viscoplastic strain tensor is normal to the tangent to yield surface):

$$\boldsymbol{\dot{\varepsilon}_{ij}^{vp}} = \frac{\partial\Omega}{\partial f}\,\frac{\partial f}{\partial\boldsymbol{\sigma_{ij}}} = \frac{3}{2}\frac{\dot{\lambda}}{(1-D)}\,\frac{\frac{\boldsymbol{\sigma'}}{1-D} - \boldsymbol{\alpha'}}{J\left(\frac{\boldsymbol{\sigma'}}{1-D} - \boldsymbol{\alpha'}\right)} \tag{7}$$

where $\boldsymbol{\alpha'}$ is the deviatoric part of the back stress tensor (an internal stress variable describing kinematic hardening); σ'represents the deviatoric part of the stress tensor; $\dot{\lambda}$ is the rate of the plastic multiplier which can be related to the rate of the effective plastic strain, $\dot{p}$, through a Norton's power law function:

$$\dot{p} = \frac{\dot{\lambda}}{1-D} = \left\langle\frac{f}{Z}\right\rangle^{n} \tag{8}$$

The parameter n is the viscoplastic exponent and controls the material's sensitivity to strain rate, while the parameter Z controls the resistance to viscoplastic deformation. In Equations (6-

8), f denotes the yield surface, which, according to von Mises yield criterion, can be defined as:

$$f = J\left(\frac{\boldsymbol{\sigma}'}{1-D} - \boldsymbol{\alpha}'\right) - R - k \tag{9}$$

In other words, the yield function f defines the elastic domain when $f \leq 0$ and the viscous stress (σ_v) when $f > 0$ (i.e., within the rate dependent plasticity framework, the current stress state may lie outside the yield surface). k represents the initial size of the yield surface while R is the drag stress (an internal stress variable describing isotropic hardening). $J\left(\frac{\boldsymbol{\sigma}'}{1-D} - \boldsymbol{\alpha}'\right)$ is the von Mises equivalent stress for the quantity $\left(\frac{\boldsymbol{\sigma}'}{1-D} - \boldsymbol{\alpha}'\right)$ as defined below:

$$J\left(\frac{\boldsymbol{\sigma}'}{1-D} - \boldsymbol{\alpha}'\right) = \sqrt{\frac{3}{2}\left(\frac{\boldsymbol{\sigma}'}{1-D} - \boldsymbol{\alpha}'\right) : \left(\frac{\boldsymbol{\sigma}'}{1-D} - \boldsymbol{\alpha}'\right)} \tag{10}$$

The UVP framework consists of kinematic hardening and isotropic hardening rules to describe the movement and scaling of the yield surface, respectively [26, 31]. In this work, an Armstrong-Frederick type kinematic hardening rule is adopted to account for the Bauschinger effect of the material, where the total back stress tensor is assumed to constitute two terms as given below:

$$\boldsymbol{\alpha} = \sum_{w=1}^{2} \boldsymbol{\alpha_w} \tag{11.a}$$

The evolution of the back stress (coupled with damage) with respect to the viscoplastic strain can be defined as a combination of a linear hardening term and a non-linear hardening (dynamic recovery) term:

$$\dot{\boldsymbol{\alpha}} = C_w \left(\frac{2}{3} a_w \, \varepsilon_{ij}^{vp} - \boldsymbol{\alpha_w} \dot{p}\right)(1-D) \tag{11.b}$$

where a_w $(w = 1, 2)$ represents the asymptotic value of the equivalent stress of the back stress $\boldsymbol{\alpha_w}$ while C_w defines the speed to reach the asymptotic value a_w.

Based on the deformation characteristics observed in our experiments (refer to Section 3.3), the following cyclic softening model is adopted to capture the tension-compression asymmetry behaviour and, therefore, enable more accurate representation of the cyclic softening [42, 44].

$$R = Q(1 - EXP(-b\lambda)) - J_m(\boldsymbol{\sigma}) \tag{12}$$

where Q is the asymptotic value of the drag stress R in the initial exponential stage of cyclic softening; b is the speed to reach the asymptotic value, Q. The term $J_m(\boldsymbol{\sigma})$ in Equation (12) incorporates the first invariant of the stress tensor as given below:

$$J_m(\boldsymbol{\sigma}) = \mu |tr(\boldsymbol{\sigma})|^l \, sgn(tr(\boldsymbol{\sigma})) \tag{13}$$

where μ and l are material constants controlling the tension-compression asymmetry; $sgn(tr(\boldsymbol{\sigma}))$ is the sign function which can be defined as follows:

$$sgn\big(tr(\boldsymbol{\sigma})\big) = \begin{cases} -1, & tr(\boldsymbol{\sigma}) < 0 \\ 0, & tr(\boldsymbol{\sigma}) = 0 \\ 1, & tr(\boldsymbol{\sigma}) > 0 \end{cases} \tag{14}$$

4.2 Physically based Damage Model

A physically based damage model is coupled within the rate-dependent framework outlined in the previous section to represent cyclic damage evolution. The modified model introduced here is based on the framework of Li and Sun *et al*. [3] for the cyclic softening of martensitic steels. The microstructural degradation mechanisms during cyclic loading are incorporated in the model as state variables, representing the lath coarsening and the annihilation of dislocation [3]. In this work, some state variables (particularly the lath coarsening model) will be modified to better describe the cyclic softening behaviour.

The damage variable is defined in terms of the evolutions of the martensite lath width and dislocation density during LCF, as shown below:

$$D = \left(\left[\frac{\delta/\delta_0}{\rho/\rho_0}\right] * \frac{1}{\varphi}\right)^{\beta} \tag{15}$$

where δ_0 is the initial martensitic lath width; δ is the martensitic lath width at a given plastic strain; ρ and ρ_0 are the dislocation density and the initial dislocation density, respectively; φ and β are material constants.

The evolution of the martensite lath width during cyclic loading is expressed in the present work as:

$$\delta = Q_\delta\,(1 - EXP(-b_\delta p)) + H_\delta p + \delta_0 \tag{16}$$

where Q_δ , b_δ and H_δ are material-dependent parameters. Q_δ is the stabilised value of the lath width in the initial exponential stage of lath coarsening; b_δ denotes the speed to reach the stabilised value Q_δ ; H_δ is a material parameter describing the stable lath coarsening.

The change in the dislocation density rate during various softening stages can be defined as:

$$\dot{\rho} = \left(k_1\sqrt{\rho} - hk_2\rho\right)\dot{p} \tag{17}$$

where $\dot{\rho}$ is the dislocation density rate; k_1 and k_2 are material constants accounting for the dislocation storage and dislocation recovery, respectively.

The term labelled h in Equation (17) is expressed in terms of the cyclic ratio L as follows:

$$h = 1 + \sinh(k_3 L)\,/k_4 \tag{18}$$

$$L = \frac{N}{N_f} \tag{19}$$

where k_3 and k_4 are material constants accounting for the accelerated reduction behaviour of dislocation density in the third stage of cyclic softening; N and N_f are the cycle number and the number of cycles at failure, respectively.

The governing equations of the damage-coupled constitutive material model are implemented within the user-defined material subroutine UMAT in ABAQUS using an implicit integration scheme.

The parameters of the UVP damage model were calibrated in previous work [1, 3] based on interrupted strain-controlled LCF tests at 600°C and TEM observations of the tested samples. In this work, the parameters obtained previously were considered as initial values and further fine-tuned based on the uniaxial load-controlled LCF tests. The optimised parameters are illustrated in Table (3).

Table (3): The Optimised UVP constitutive model for the FV566 steel at 600°C

Parameter Scopes	Material Parameters	Values
Elastic	E_0 (MPa)	96,110
	k (MPa)	168.32
	v	0.3
Isotropic hardening	Q (MPa)	-105.87
	b	1.52
	μ	3.9×10^{-8}
	l	3.0
Kinematic hardening	a_1 (MPa)	149.96
	C_1	16.86
	a_2 (MPa)	85.23
	C_2	105.82
Viscosity (Creep)	Z (MPa)	48195.51
	n	1.76
Damage	φ	76.92
	β	0.68
	Q_δ (μm)	0.079
	b_δ	14.9
	H_δ	0.3
	k_1	6.6×10^7
	k_2	5.85
	k_3	8.8
	k_4	7800

5. DISCUSSION

In this Section, the Finite Element results (Section 5.1) will be analysed and discussed in conjunction with the results from the microstructural investigation (Section 5.2) in order to interpret the macroscopic observations from the cyclic tests and hence facilitate an in-depth understanding of the underlying cyclic degradation mechanisms.

5.1 Finite Element (FE) Results

To assess the capability of the microstructure-informed constitutive material model for the prediction of the cyclic softening and the relevant physical behaviour, the uniaxial and multi-axial load-controlled LCF tests are simulated using ABAQUS user material subroutine UMAT, and the predicted results are compared with the experimental measurements of the FV566 steels at 600°C. The uniaxial cyclic viscoplasticity analysis results are presented in Section 5.1.1, while those relevant to the multi-axial stress state are shown in Section 5.1.2.

5.1.1 Uniaxial Cyclic Behaviour

The cyclic deformation and damage behaviour of the FV566 steels under uniaxial load-controlled LCF were simulated using the physically based damage-coupled VP model. The FE model used in the uniaxial LCF analysis consists of one 3D cubic element (designated as C3D8 in ABAQUS). The predicted stress-strain responses, under uniaxial load-controlled LCF testing, at different fatigue life stages are compared with the experimental data as presented in Fig.9. As can be seen, the model successfully predicts the hysteresis response and the progressive shift of the hysteresis loops. Strain evolutions during cycling under different loading conditions are also predicted and compared with the corresponding experimental data, as shown in Figs.10. The model satisfactorily predicts the three stages of cyclic softening (Fig.10a) and the ratcheting rates, $\frac{d\varepsilon_r}{dN}$, (Fig.10b). A key advantage of the micromechanical physically based model manifests in that it can predict not only the macroscopic LCF behaviour but also the associated microstructure evolution during stress cycling such as the annihilation of dislocations, as depicted in Fig.11. (The initial dislocation density ($3.1x10^{14}$ m^{-2}) has been measured in a previous investigation based on TEM characterisation of the as-received steel [2]). The evolution of dislocation densities for the FV566 steel during high-temperature cyclic softening follows three stages, namely; Stage 1, with a sharp decrease in dislocation density, Stage 2, with a stable reduction and finally Stage 3, with a rapid decrease in dislocation density.

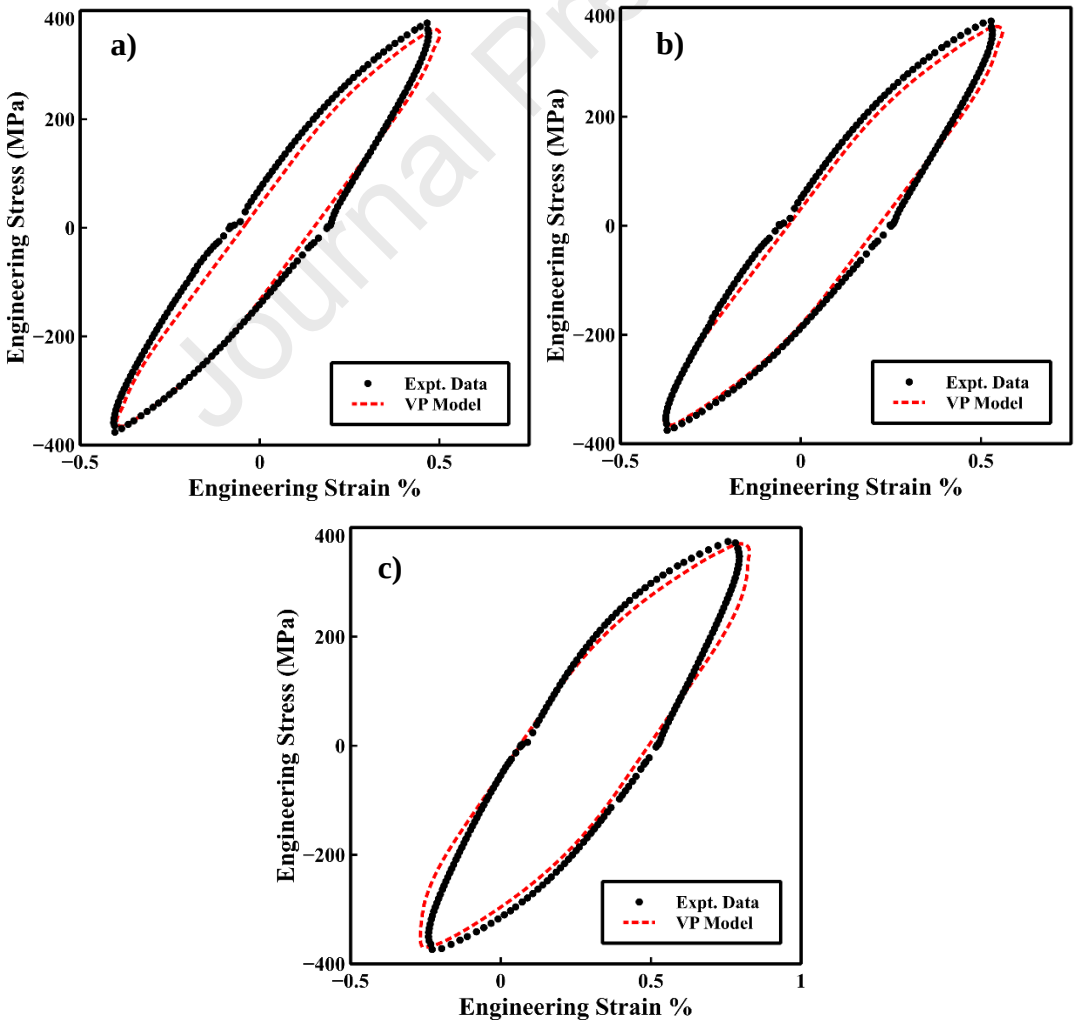

Fig.9: Comparison of the experimental and simulated hysteresis response of the FV566 'plain bar' at 600°C subjected to 7360N uniaxial load-controlled LCF at different fatigue life stages, namely a) 20 cycles, b) 40 cycles, and c) 100 cycles.

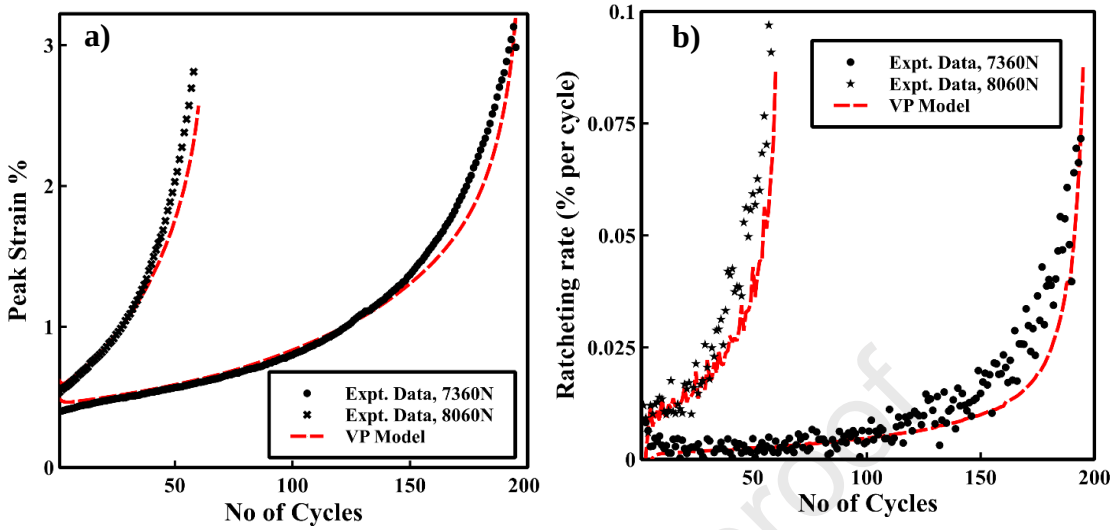

Fig.10: Comparison of the experimental and predicted strain softening behaviour of the FV566 'plain bar' at 600°C under uniaxial load-controlled cyclic conditions. The cyclic softening is presented herein in terms of a) Peak strain evolution, and b) The ratcheting rates.

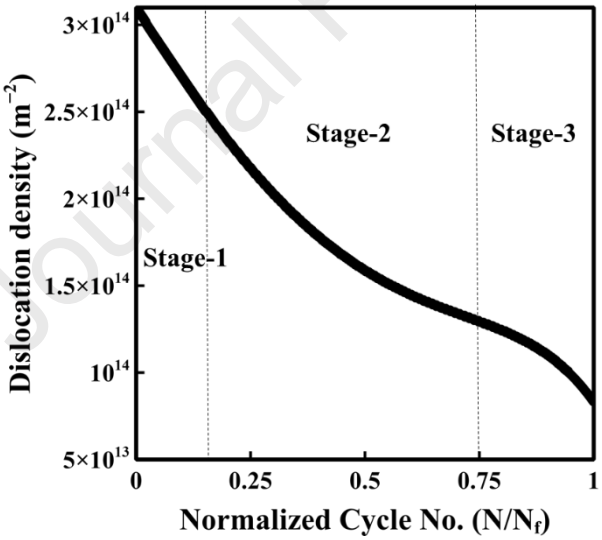

Fig.11: The FE predicted evolutions of the dislocation density under 7360N uniaxial 'plain bar' load-controlled LCF testing.

Based on TEM characterisation of the failed specimens, the microstructural characteristics related to cyclic damage such as lath width and dislocation density are measured at failure state and compared against those obtained from the physically-based damage model as shown in Table (4).

It should be noted that the average dislocation density (ρ) within grain interior is estimated following the line intercept method [49] as follows:

$$\rho = \frac{N}{L_r\, t} \tag{20}$$

where, N is the number of intersection points; L_r is the total length of the random lines, and t is the foil thickness.

Table (4): Comparison of the measured and predicted microstructural characteristics under 7360N uniaxial 'plain bar' load-controlled LCF test.

Microstructural variable	TEM Measurements	FE Model Prediction
Lath width (μm)	0.65	0.89
Dislocation density (m^{-2})	$0.98x10^{14}$	$0.8x10^{14}$

5.1.2 Multiaxial Cyclic Behaviour

The VP damage model was implemented to simulate the isothermal load-controlled notched bar tests. The geometrical details of the notched bar specimen are as follows: notch radius=0.5mm; gauge length=10mm; maximum gauge diameter=5mm. Due to the symmetry of the problem, only a quarter of the geometry was modelled using symmetry boundary conditions, as shown in Fig.12. The FE model of the notched bar consists of 484 bilinear axisymmetric elements (designated as CAX4 in ABAQUS). Finer mesh discretisation was applied at the notch region, where stresses and strains are expected to vary rapidly. The results from the FE analysis of the notched bars are shown in the following subsections.

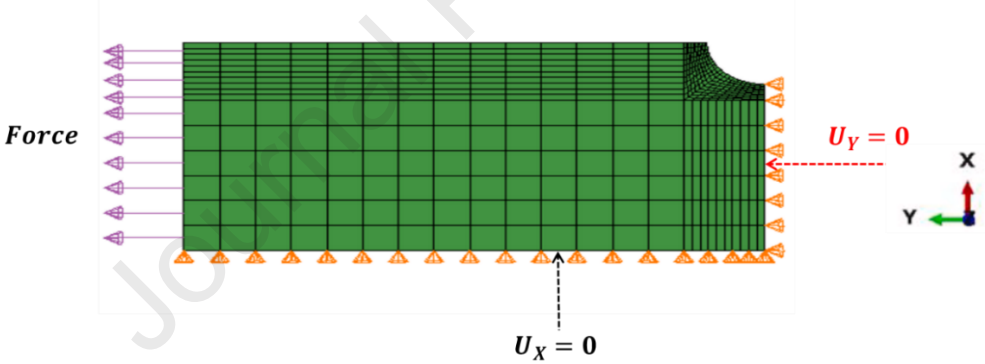

Fig.12: FE model of the notched bar

5.1.2.1 Localised Stresses and Notch Strengthening

The FE stress analysis on the notched bar can help us derive insights into the effect of constraints on the LCF performance. In Fig.13, we show the predicted effective stress, σ_{equiv}, distribution in the notched bar tested under 7360N load-controlled conditions after 207 cycles. A highly localised stress can be observed close to the notch root. However, the stresses developed across the notch plane appear to redistribute below the applied mean axial (nominal) stress (σ_0), which partially explains the notch-strengthening behaviour observed in our experiments (refer to Table (2)). The stress relaxation behaviour in the notched bar also seems to be responsible for the lower degrees of ratcheting observed in the notched bar LCF tests as opposed to the uniaxial tests at the same stress level (Fig.7a).

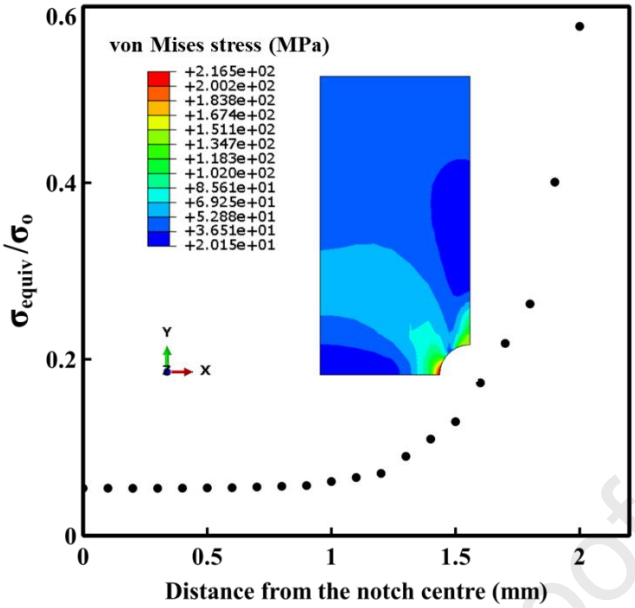

Fig.13: Notched bar stress analysis results under 7360N load-controlled LCF testing showing contour plot of the von Mises equivalent stress distribution in the specimen and the ratio of the effective stress, σ_{equiv}, to the applied nominal stress, σ_0, along the notch radius. (Results obtained after 207 cycles).

5.1.2.2 Localised Plasticity and Damage

The local plastic strain can serve as an indicator of the extent of cyclic plasticity damage. The predicted maximum principal strains across the notch plane at different fatigue lives are shown in Fig.14. Similar to the notched bar local stresses pattern, local strains tend to increase as we move closer to the notch root. Further, an increase in the local strain with cycles (ratcheting) can be observed, as illustrated in Fig.14. A higher level of viscoplasticity damage is predicted to occur closer to the notch root, as shown in Fig.15a, due to the stress and strain localisations at this region. SEM results reveal crack initiation at the notch root, which agrees with the VP modelling results. In order to better understand the damage localisation at the notch root, the microdamage modelling results, showing dislocation density pattern, across the notch bar throat plane at failure are acquired and plotted in Fig.15b. As shown, the model reveals higher dislocation annihilation at the notch root than at the centre of the notched bar, and thereby leading to more damage and causing crack initiation at the notch root. Interestingly, dislocation densities across the notch throat plane at failure are predicted to be higher than those obtained for the uniaxial plain bar at the same cyclic loading conditions. This could indicate a higher fatigue strength for the material under multi-axial LCF than under uniaxial conditions, possibly contributing to the notch-strengthening effect observed in our experiments.

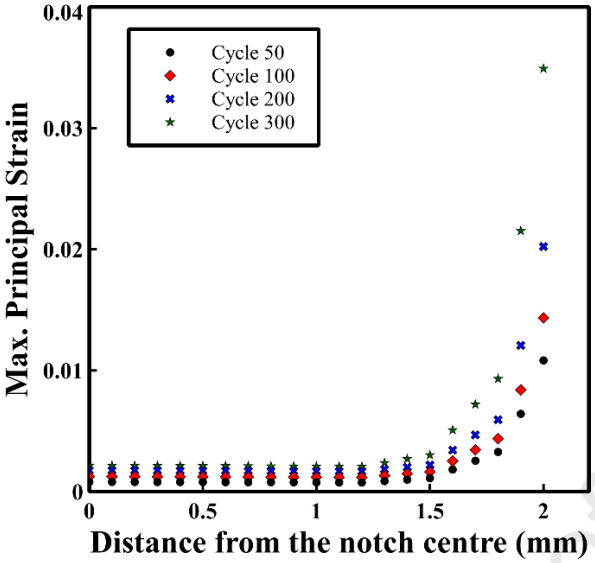

Fig.14: Maximum principal strain variation along the notch radius at different fatigue cycles obtained from the VP damage analysis on the notched bar tested under 7360N uniaxial load-controlled LCF.

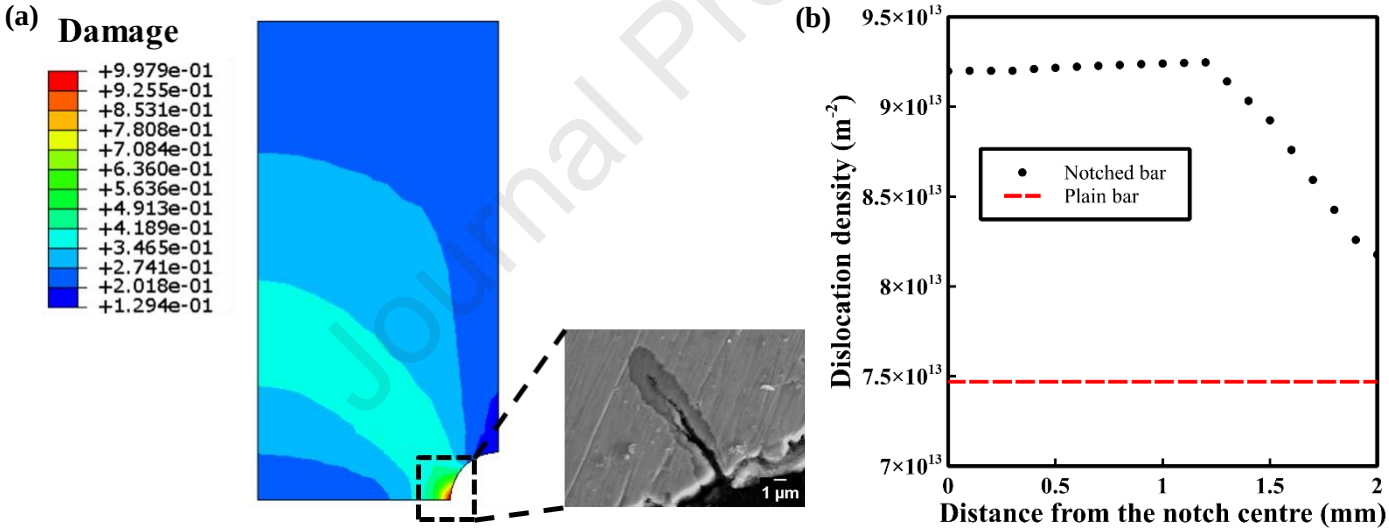

Fig.15: Physically-based damage modelling results showing a) The predicted viscoplasticity damage variable close to failure in the notched bar LCF test subjected to 7360N load-controlled cyclic loading and the corresponding SEM image showing crack initiation close to the notch root, and b) The predicted dislocation densities pattern [in m^{-2}] at failure, across the notch throat plane as compared to the uniaxial plain bar.

5.1.2.3 Notched Bar Softening Behaviour

The predicted peak strain evolution with cycles and stress-strain response during the first cycle are shown in Fig.16a and Fig.16b, respectively for a notched bar LCF test. Although the model accurately predicts the softening behaviour in the first two stages (Fig.16a), it underestimates strain evolution in the tertiary stage. This could suggest that the damage model needs to be improved under multi-axial stress state conditions to overcome this limitation. Some potential

mechanisms which have not been included in the current VP model but might be operative are discussed in Section 5.2.3.

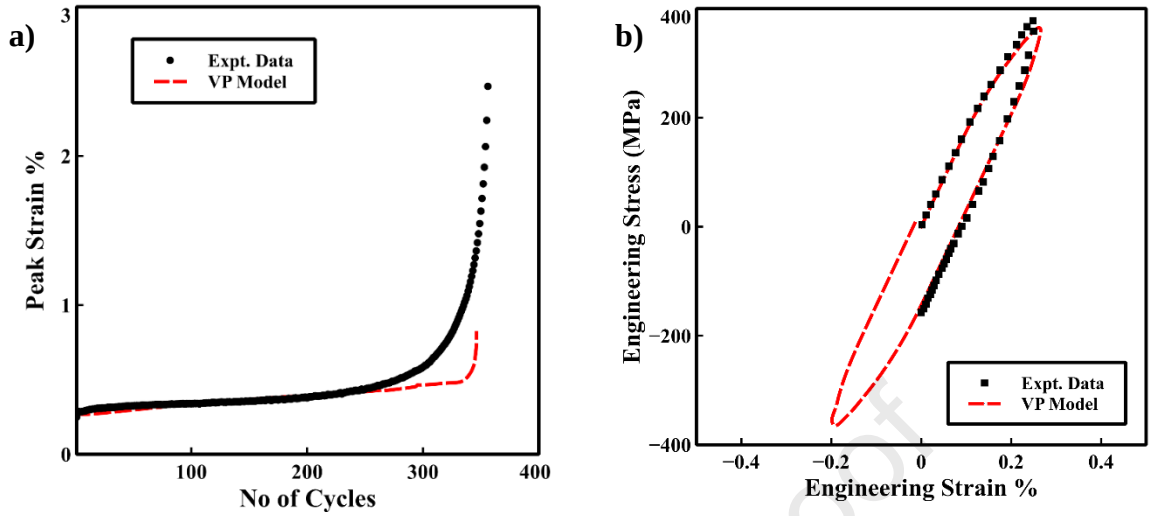

Fig.16: Comparison of the notched bar simulation results with the experimental data under 7360N load controlled LCF, showing: a) evolution of peak strain, and b) stress-strain cyclic response

5.2 Microdamage and Cyclic Softening Mechanisms

In this Section, the cyclic deformation characteristics will be analysed in conjunction with the results from the microstructural investigation to better understand the ratcheting and constraint effects on fatigue fracture mechanisms and the associated microstructural damage evolutions in FV566 steels at high temperatures.

5.2.1 Fatigue Fracture Mechanism

The fracture surfaces of the tested samples were examined using SEM to unravel some insights into the fatigue fracture mechanisms. For the investigated material, fatigue fracture is thought to be related to micro-void formation and coalescence into micro-cracks. Some of these voids are associated with inclusions (shown in Fig.17a), which can be regarded as potential sites for fatigue crack nucleation. Voids may have nucleated due to the particle-matrix decohesion mechanism, which can be attributed to stress concentration arising from dislocation pile-up at the inclusions [5]. Based on the EDS analysis, the compositions of these inclusions are revealed, as shown in Fig.17b, which are primarily aluminium oxides.

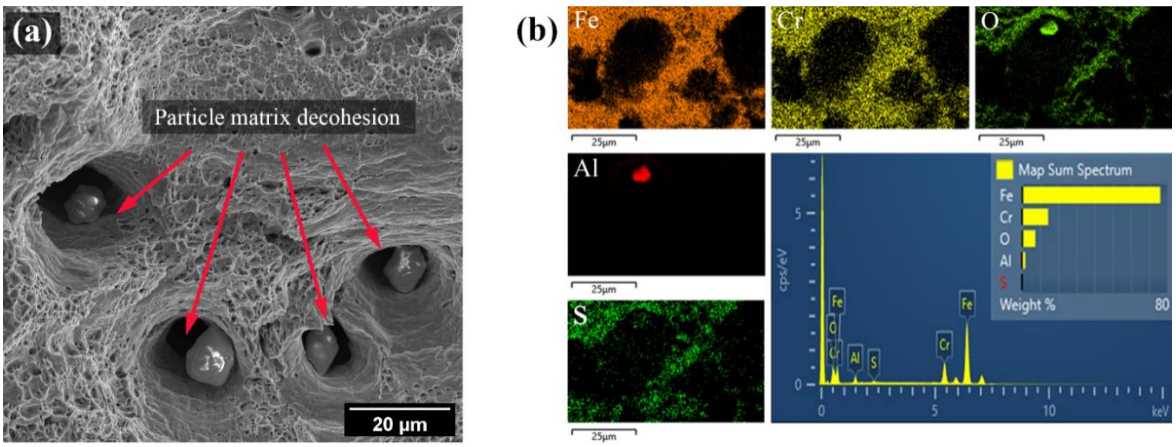

Fig.17: SEM/EDS analysis of the fracture surface of the tested FV566 steel sample at 600°C, showing some defects contributing to LCF damage. a) Particle-Matrix decohesion, and b) Analysis of the chemical compositions of the defects.

5.2.2 Effects of Constraint on Fatigue Fracture Mode

To identify the effects of constraint on fatigue fracture characteristics, the fracture behaviour of the plain bar (i.e., under a uniaxial stress state) is compared to the corresponding behaviour of the notched bar for the same cyclic mechanical conditions. As shown in Fig.18a, a cup-cone type fracture can be observed at the macro level for the plain bar tested under uniaxial load-controlled cyclic conditions, implying a ductile-dominated failure. This is also supported by the dimple-dominated fracture surface appearance, which can be observed under the uniaxial load-controlled LCF, as shown in Fig.18b. Such characteristics indicate the transgranular ductile failure mode. Moreover, micro-voids appear to have rotated and elongated in a preferential direction during deformation, as depicted in Fig.18c, which may suggest a shear-dominated rupture. On the other hand, the notched bar shows a comparatively lower degree of necking (Fig.19a) and different fracture morphologies. While the fracture is dimple dominated at the notch centre (Fig.19c), the density of these dimples decreases closer to the notch root, as illustrated in Fig.19b. Fatigue striations and micro-cracking can also be observed closer to the notch root, as shown in Fig.19b, indicating crack initiation at the notch root, which is in consistency with the viscoplasticity damage modelling results presented in Fig.15a. Comparing the fracture surface appearance of the notched bar (Fig.18a) to that of the plain (unnotched) bar (Fig.19a) shows that the notched bar has a relatively flat fracture surface (i.e., the fracture surface is almost perpendicular to the loading axis), which possibly indicates a mode-I dominated fracture. On this basis, fatigue notch strengthening in notched bar tests can be correlated with the transition in fatigue fracture behaviour from shear to mode-I dominated rupture. Similar observations on the link between notch strengthening and transition in failure mode were noted previously by [50]. The notch constraint is also shown to influence the micro-void shape. Due to the multi-axial stress state in the notched bar, voids grow uniformly in all directions as can be inferred from the spherical-like shape shown in Fig.19d, as opposed to the elongated void shape under uniaxial stress state shown in Fig.18c.

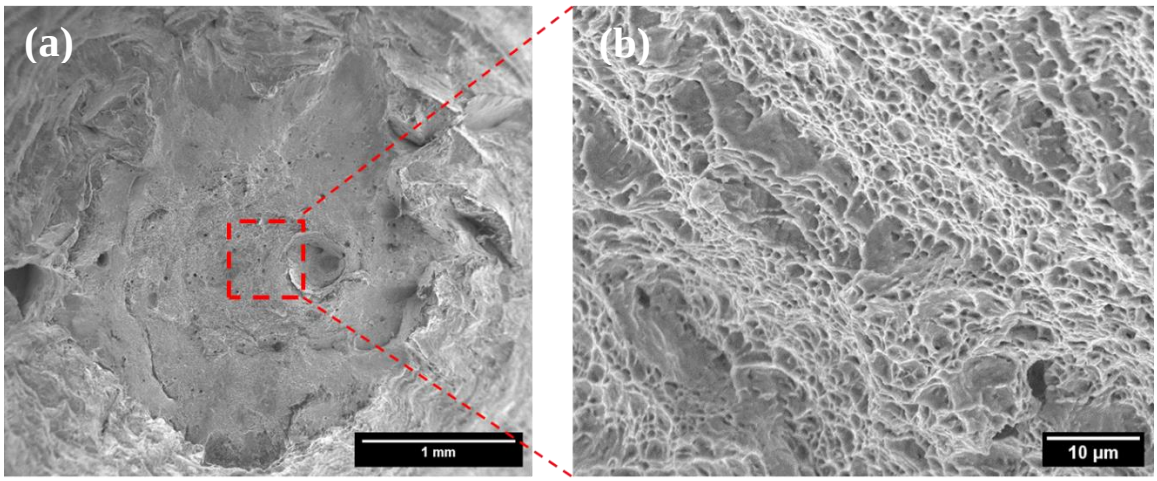

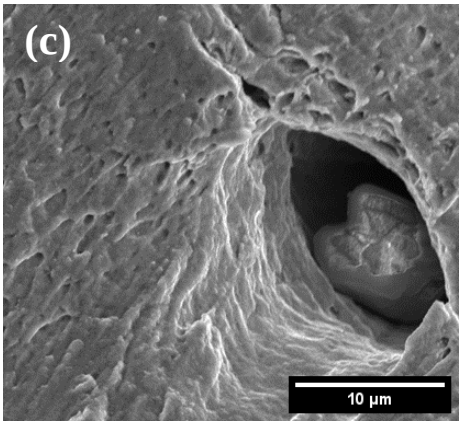

Fig.18: SEM images showing the fracture surface of the ruptured plain bar tested under 7360N load-controlled LCF at 600°C. a) Fracture surface appearance at the macro level, and b) Magnified view showing the fracture morphology of the tested sample at a selected region, and c) Distortion of void shape due to shear stress.

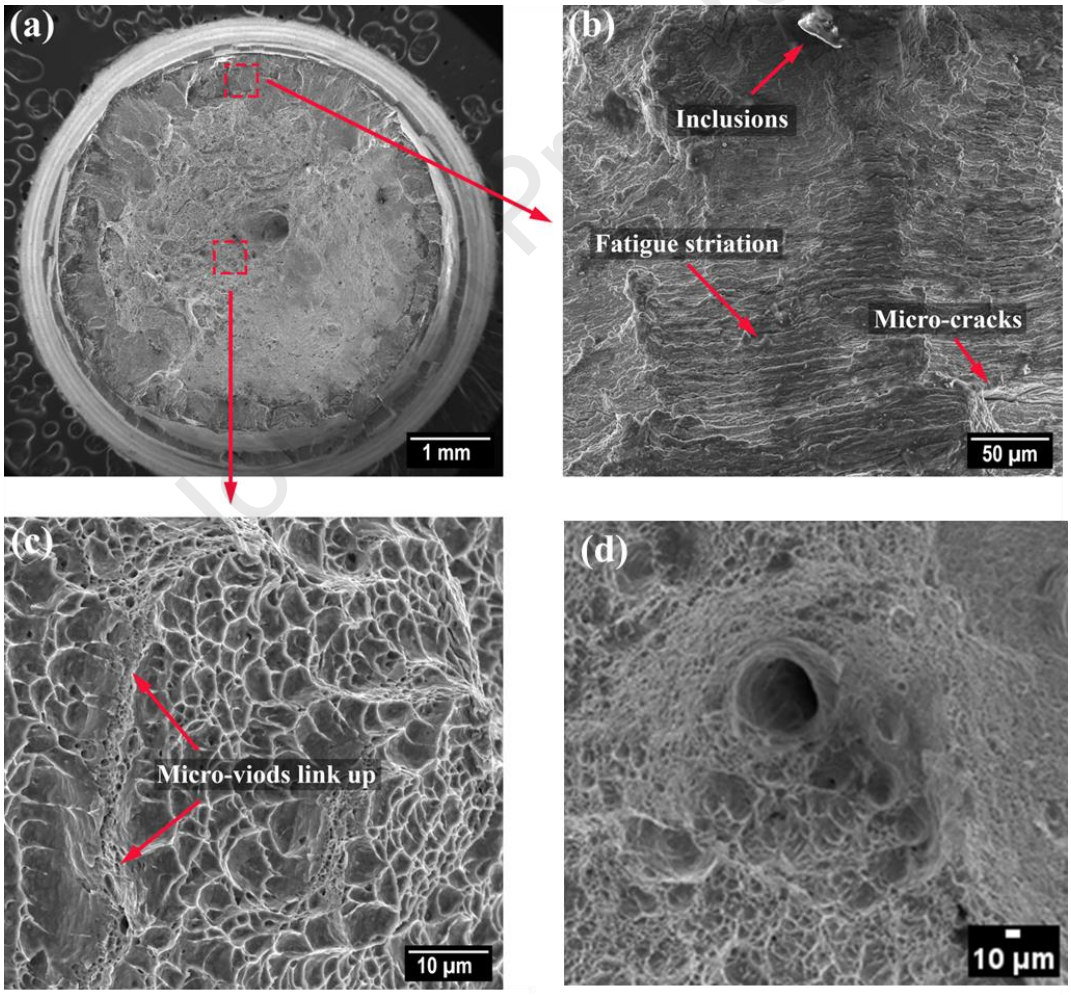

Fig.19: SEM images showing the fracture surface of the ruptured notched bar tested under 7360N load-controlled LCF at 600°C. a) Fracture surface at the macro-level; b) Magnified view showing fracture morphology at a selected region close to the notch root; c) Magnified view showing fracture morphology at the notch centre; d) A spherical-like void present at the centre of the notched bar fracture surface.

5.2.3 Ratcheting and Constraint Effects on Microstructure Recovery

In this Section, we will examine the microstructural changes associated with cyclic softening (ratcheting) under load-controlled cyclic tests at the subgrain level. In particular, the effect of constraints on the substructure recovery will be clarified based on TEM analysis. In the as-received state (shown in Fig.20a and Fig.20b), the FV566 steel exhibits a tempered martensitic structure with a relatively high dislocation density and a dispersion of fine precipitates. However, following load-controlled LCF testing, a remarkable subgrain coarsening can be observed accompanied by the annihilation of the low-angle grain boundary dislocations, as shown in Fig.20c and Fig.20d, respectively. The annihilation process during LCF might be related to the increased emigration of dislocations along the subgrain boundary and wall [15]. Pile-up of dislocations at low angle grain boundaries (LAGBs) can be observed in Fig.20d. When the pile-up reaches a critical state, it can result in the formation of dislocation walls [45], as shown in Fig.20c. This could lead to stress concentrations at the lath boundary and the subsequent fragmentation of the lath structure into equiaxed subgrains. Since the microstructural heterogeneities in the material (e.g., dislocations, grain boundaries, etc) are known to be the source of kinematic hardening, the ratcheting-induced microstructural changes such as the subgrain coarsening and dislocation annihilation can, therefore, rationalise the decrease in the back stress observed in our cyclic mechanical tests, as illustrated earlier in Fig.8b.

The subgrain recovery in terms of lath transformation into larger cells and dislocation density reduction within the lath interior can also be noticed for the notched bar sample, as shown in Figs.20e-j. Nonetheless, compared to the microstructural evolution under the uniaxial stress state, the precipitate coarsening behaviour appears to be more pronounced under the multi-axial stress state, as illustrated in Figs.20e-f. Carbide coarsening could further ease the dislocation movement due to the reduced pinning effect and thereby resulting in cyclic softening. This implies that in multi-axial LCF tests, cyclic softening may occur not only by lath coarsening and LAGBs dislocations annihilation but also by precipitates coarsening.

In order to provide mechanistic insights that could aid in the understanding of fatigue notch strengthening behaviour in multi-axial notched bar LCF tests, we compare dislocation structure in the material under both uniaxial and multi-axial stress states. TEM shows a qualitatively higher density of dislocation tangles within the subgrains across the notched bar fracture surface (Figs.20h, j) than in the uniaxial plain bar (Fig.20d), which is consistent with the FE micro-damage modelling results (Fig.15b) and the macroscopic observations (Fig.7b), indicating improved fatigue strength with the introduction of notches, and thereby longer fatigue lives.

To examine the extent of substructure recovery and damage localisation across the notch bar throat plane, we compare the TEM results at two local points, namely at the notched bar root (Fig.20g-h) and at the notched bar centre (Fig.20i-j). It can be shown that considerably higher dislocation annihilation and more substructure growth due to subgrain boundary migration occur at the notched bar root than at the centre, which can explain the damage localisation predicted by the FE damage model and crack initiation found at the notch root (Fig.15a).

As received material

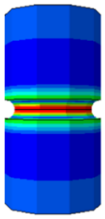

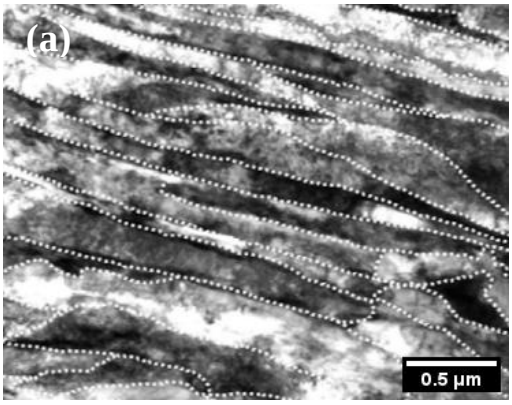

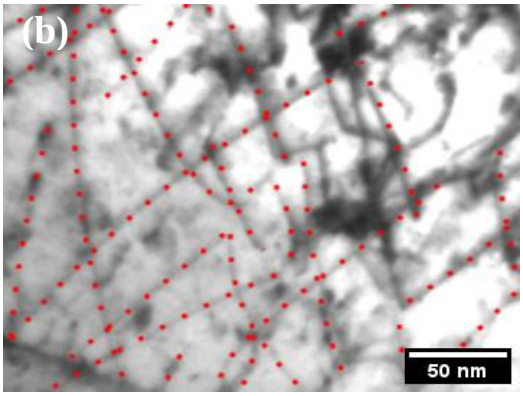

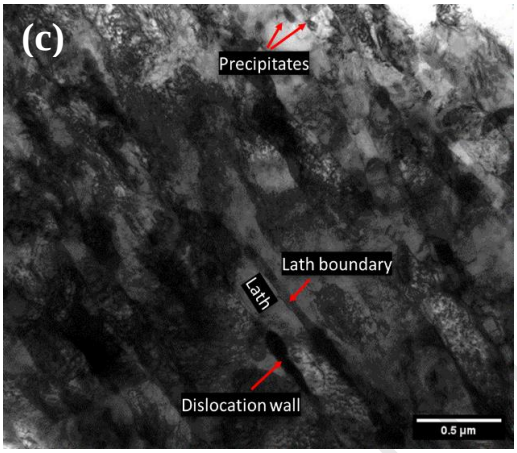

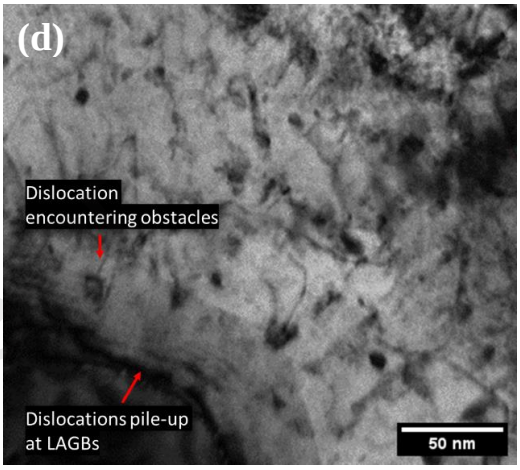

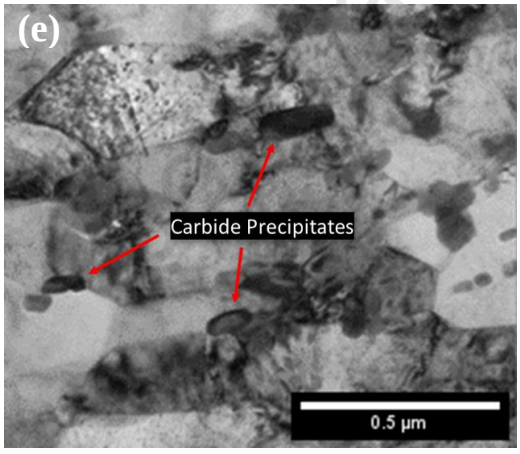

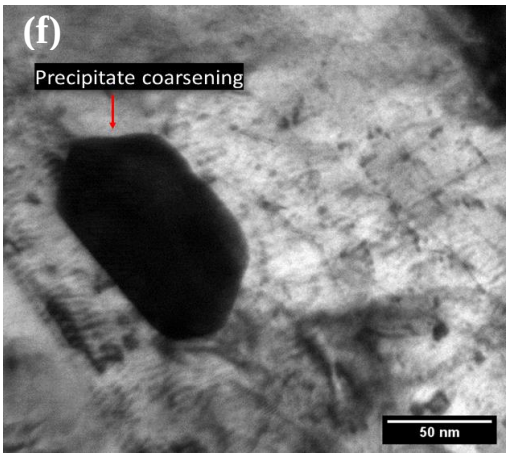

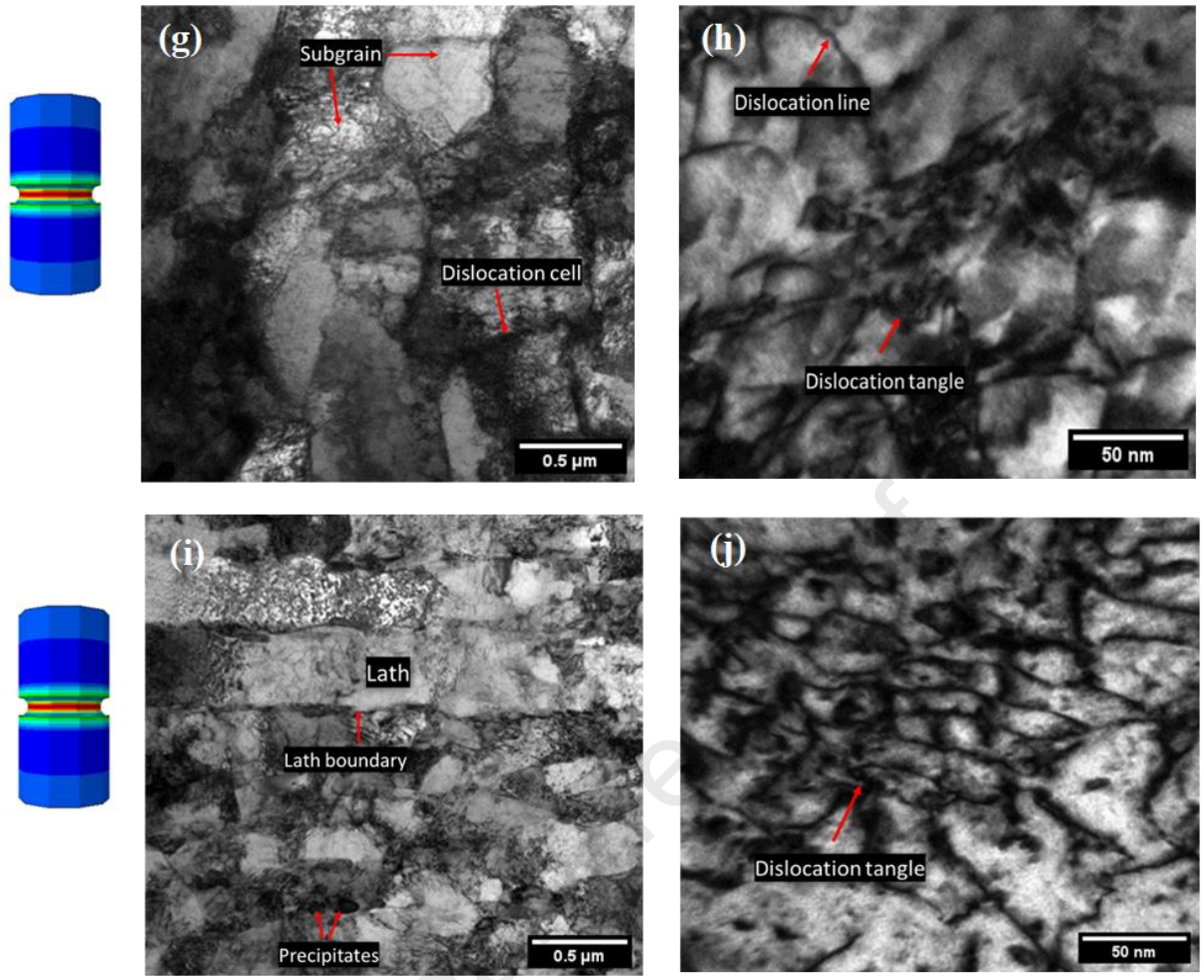

Fig.20: TEM images at the fracture surface of the FV566 plain bars and notched bars tested under load-controlled LCF at 600ºC as compared to the as-received state. a), b) Microstructure of the FV566 steels in the as-received state [2]; c), d) TEM observations of the LCF tested uniaxial plain bars; e), f) TEM images showing the precipitate coarsening behaviour under multi-axial stress state; g), h) TEM images taken at the notched bar root; i), j) TEM observations at the notched bar centre.

6. CONCLUSION AND FUTURE WORK

In this work, the effects of ratcheting and constraint on the low cycle fatigue performance of FV566 steels at high temperatures were systematically investigated by employing experimental and theoretical approaches. The theoretical work combined with microstructural characterisation (SEM and TEM analysis) advanced our understanding of the failure mode and the key mechanisms contributing to the cyclic viscoplasticity damage in FV566 steels at high temperatures. The key findings from the present study can be concluded as follows:

- Ratcheting was observed under zero mean stress, and this behaviour was related to the incomplete reversibility of plastic deformations during loading cycles.
- The modified physically based model showed an excellent capability to predict the cyclic viscoplasticity behaviour and the associated microstructural degradation mechanisms.

- Based on SEM/EDS analyses of the LCF-tested samples, inclusions in the material contributed to micro-void nucleation and the subsequent fatigue crack initiation.
- The ratcheting observed experimentally under load-controlled LCF induced significant microstructural changes at the subgrain level such as the decomposition of martensite laths into larger cells, reductions in dislocation densities within laths and carbide precipitates coarsening.
- Due to the presence of constraint, a transition in fatigue fracture behaviour from ductile shear-dominated failure to mode-I fracture was observed. Fatigue notch strengthening in notched bar cyclic tests was correlated with this transition.
- At the micro-scale, the beneficial effect of the notch constraint on fatigue life (notch strengthening) was rationalised on the basis of the higher dislocation densities retained in the material under multi-axial LCF than under uniaxial conditions.
- Under multi-axial stress states, the contribution of precipitates coarsening to cyclic softening was more pronounced.

Driven by the microscopic observations from this study, further refinement is needed to improve the predictive capability of the physically based damage model, particularly under multi-axial loading conditions. This could include the incorporation of the precipitate coarsening mechanism into the current model. For this purpose, interrupted LCF tests under stress-controlled conditions are required. This will be addressed in our future work. Equally important is the effect of crystallographic orientations on the cyclic deformation and softening behaviour, which will be explored later using multi-scale modelling tools such as crystal plasticity-based models. To further study the effect of constraint on fatigue crack growth, phase field damage modelling coupled with visco-plasticity could present an effective option.

ACKNOWLEDGMENTS

This work was supported by the Engineering and Physical Sciences Research Council (EPSRC). The funding is provided through the EPSRC Centre for Doctoral Training in Resilient Decarbonised Fuel Energy Systems (Grant number: EP/S022996/1). The work was also partly sponsored by the Net Zero Research. The authors thank the Nanoscale and Microscale Research Centre (nmRC) at University of Nottingham for providing access to SEM and TEM instrumentation. This work was also supported by the Engineering and Physical Sciences Research Council (EPSRC) [under grants EP/L022494/1 and EP/S0214334/1] and the University of Nottingham. The authors gratefully acknowledge the University of Nottingham's High-Performance Computing (HPC) facility.

REFERENCES

1. Rae, Y., Benaarbia, A., Hughes, J. and Sun, W., 2019. Experimental characterisation and computational modelling of cyclic viscoplastic behaviour of turbine steel. *International Journal of Fatigue*, *124*, pp.581-594.
2. Rae, Y., Guo, X., Benaarbia, A., Neate, N. and Sun, W., 2020. On the microstructural evolution in 12% Cr turbine steel during low cycle fatigue at elevated temperature. *Materials Science and Engineering: A*, *773*, p.138864.
3. Li, D.H., Li, M., Shang, D.G., Gupta, A. and Sun, W., 2021. Physically-based modelling of cyclic softening and damage behaviors for a martensitic turbine rotor material at elevated temperature. *International Journal of Fatigue*, *142*, p.105956.
4. Zhao, P., Xuan, F.Z. and Wang, C., 2019. A physically-based model of cyclic responses for martensitic steels with the hierarchical lath structure under different loading modes. *Journal of the Mechanics and Physics of Solids*, *124*, pp.555-576.
5. O'Hara, E.M., Harrison, N.M., Polomski, B.K., Barrett, R.A. and Leen, S.B., 2017. Fatigue damage characterisation of MarBN steel for high temperature flexible operating conditions. *Proceedings of the Institution of Mechanical Engineers, Part L: Journal of Materials: Design and Applications*, *231*(1-2), pp.23-37.
6. Benaarbia, A., Xu, X., Sun, W., Becker, A.A. and Osgerby, S., 2020. Characterisation of cyclic behavior, deformation mechanisms, and microstructural evolution of MarBN steels under high temperature conditions. *International Journal of Fatigue*, *131*, p.105270.
7. Lu, J., Sun, W., Becker, A. and Saad, A.A., 2015. Simulation of the fatigue behaviour of a power plant steel with a damage variable. *International Journal of Mechanical Sciences*, 100, pp.145-157.
8. Kyaw, S.T., Rouse, J.P., Lu, J. and Sun, W., 2016. Determination of material parameters for a unified viscoplasticity-damage model for a P91 power plant steel. *International Journal of Mechanical Sciences*, 115, pp.168-179.
9. Kannan, R., Sankar, V., Sandhya, R. and Mathew, M.D., 2013. Comparative evaluation of the low cycle fatigue behaviours of P91 and P92 steels. *Procedia Engineering*, *55*, pp.149-153.
10. Saad, A.A., Hyde, T.H., Sun, W., Hyde, C.J. and Tanner, D.W., 2013. Characterisation of viscoplasticity behaviour of P91 and P92 power plant steels. *International Journal of Pressure Vessels and Piping*, *111*, pp.246-252.
11. Sauzay, M., Brillet, H., Monnet, I., Mottot, M., Barcelo, F., Fournier, B. and Pineau, A., 2005. Cyclically induced softening due to low-angle boundary annihilation in a martensitic steel. *Materials Science and Engineering: A*, *400*, pp.241-244.
12. Fournier, B., Dalle, F., Sauzay, M., Longour, J., Salvi, M., Caës, C., Tournié, I., Giroux, P.F. and Kim, S.H., 2011. Comparison of various 9–12% Cr steels under fatigue and creep-fatigue loadings at high temperature. *Materials Science and Engineering: A*, *528*(22-23), pp.6934-6945.
13. Zhang, S.L. and Xuan, F.Z., 2017. Interaction of cyclic softening and stress relaxation of 9–12% Cr steel under strain-controlled fatigue-creep condition: Experimental and modeling. *International Journal of Plasticity*, *98*, pp.45-64.
14. Jing, H., Luo, Z., Xu, L., Zhao, L. and Han, Y., 2018. Low cycle fatigue behavior and microstructure evolution of a novel 9Cr–3W–3Co tempered martensitic steel at 650° C. *Materials Science and Engineering: A*, *731*, pp.394-402.

15. Zhang, H., Wang, Q., Gong, X., Wang, T., Pei, Y., Zhang, W., Liu, Y., Wang, C. and Wang, Q., 2021. Comparisons of low cycle fatigue response, damage mechanism, and life prediction of MarBN steel under stress and strain-controlled modes. *International Journal of Fatigue*, *149*, p.106291.
16. Wu, D.L., Zhao, P., Wang, Q.Q. and Xuan, F.Z., 2015. Cyclic behavior of 9–12% Cr steel under different control modes in low cycle regime: A comparative study. *International Journal of Fatigue*, *70*, pp.114-122.
17. Paul, S.K., 2019. A critical review of experimental aspects in ratcheting fatigue: microstructure to specimen to component. *Journal of Materials Research and Technology*, *8*(5), pp.4894-4914.
18. Zhang, B., Rongqiao, W.A.N.G., Dianyin, H.U., Jiang, K., Jianxing, M.A.O., Fulei, J.I.N.G. and Xinyi, H.A.O., 2021. Stress-controlled LCF experiments and ratcheting behaviour simulation of a nickel-based single crystal superalloy with [001] orientation. *Chinese Journal of Aeronautics*, *34*(8), pp.112-121.
19. Feaugas, X. and Gaudin, C., 2004. Ratchetting process in the stainless steel AISI 316L at 300 K: an experimental investigation. *International Journal of Plasticity*, *20*(4-5), pp.643-662.
20. Ragab, R., Parker, J., Li, M., Liu, T., Morris, A. and Sun, W., 2022. Requirements for and challenges in developing improved creep ductility-based constitutive models for tempered martensitic CSEF steels. *journal of materials research and technology*.
21. Goyal, S. and Laha, K., 2014. Creep life prediction of 9Cr–1Mo steel under multi-axial state of stress. *Materials Science and Engineering: A*, *615*, pp.348-360.
22. Goyal, S., Laha, K., Das, C.R., Panneerselvi, S. and Mathew, M.D., 2014. Effect of constraint on creep behavior of 9Cr-1Mo steel. *Metallurgical and Materials Transactions A*, *45*(2), pp.619-632.
23. Chang, Y., Xu, H., Ni, Y., Lan, X. and Li, H., 2015. The effect of multi-axial stress state on creep behavior and fracture mechanism of P92 steel. *Materials Science and Engineering: A*, *636*, pp.70-76.
24. Niu, T.Y., Zhao, P., Zhu, G., Gong, J.G. and Xuan, F.Z., 2021. Stress state dependent creep damage behavior of 9–12% Cr steel notched components. *Materials Science and Engineering: A*, *804*, p.140762.
25. Xu, X., Wang, G.Z., Xuan, F.Z. and Tu, S.T., 2016. Effects of creep ductility and notch constraint on creep fracture behavior in notched bar specimens. *Materials at High Temperatures*, *33*(2), pp.198-207.
26. Chaboche, J.L., 2008. A review of some plasticity and viscoplasticity constitutive theories. *International journal of plasticity*, *24*(10), pp.1642-1693.
27. Benaarbia, A., Rae, Y. and Sun, W., 2018. Unified viscoplasticity modelling and its application to fatigue-creep behaviour of gas turbine rotor. *International Journal of Mechanical Sciences*, *136*, pp.36-49.
28. Ahmed, R., Barrett, P.R. and Hassan, T., 2016. Unified viscoplasticity modeling for isothermal low-cycle fatigue and fatigue-creep stress–strain responses of Haynes 230. *International Journal of Solids and Structures*, *88*, pp.131-145.
29. Chen, W., Wang, F. and Feng, M., 2017. Study of a modified non-unified model for time-dependent behavior of metal materials. *Mechanics of Materials*, *113*, pp.69-76.
30. Chaboche, J.L. and Rousselier, G., 1983. On the plastic and viscoplastic constitutive equations—Part I: Rules developed with internal variable concept.

31. Chaboche, J.L., 1989. Constitutive equations for cyclic plasticity and cyclic viscoplasticity. *International journal of plasticity*, *5*(3), pp.247-302.
32. Chaboche, J.L., 1988. Continuum damage mechanics: Part I—General concepts.
33. Lemaitre J, Desmorat R. *Engineering damage mechanics: Ductile, creep, fatigue and brittle failures*, Netherlands: Springer Science & Business Media, 2005.
34. Barrett, R.A., O'Donoghue, P.E. and Leen, S.B., 2017. A physically-based constitutive model for high temperature microstructural degradation under cyclic deformation. *International Journal of Fatigue*, *100*, pp.388-406.
35. Sauzay, M., Fournier, B., Mottot, M., Pineau, A. and Monnet, I., 2008. Cyclic softening of martensitic steels at high temperature—Experiments and physically based modelling. *Materials Science and Engineering: A*, *483*, pp.410-414.
36. Führer, U. and Aktaa, J., 2018. Modeling the cyclic softening and lifetime of ferritic-martensitic steels under creep-fatigue loading. *International Journal of Mechanical Sciences*, *136*, pp.460-474.
37. Kreethi, R., Sivateja, C., Mondal, A.K. and Dutta, K., 2019. Ratcheting life prediction of quenched–tempered 42CrMo4 steel. *Journal of Materials Science*, *54*(17), pp.11703-11712.
38. Zhu, S.P., Lei, Q. and Wang, Q.Y., 2017. Mean stress and ratcheting corrections in fatigue life prediction of metals. *Fatigue & Fracture of Engineering Materials & Structures*, *40*(9), pp.1343-1354.
39. Chang, L., Wen, J.B., Zhou, C.Y., Zhou, B.B. and Li, J., 2018. Uniaxial ratcheting behavior and fatigue life models of commercial pure titanium. *Fatigue & Fracture of Engineering Materials & Structures*, *41*(9), pp.2024-2039.
40. Liu, Y., Kang, G. and Gao, Q., 2008. Stress-based fatigue failure models for uniaxial ratchetting–fatigue interaction. *International journal of fatigue*, *30*(6), pp.1065-1073.
41. Yaguchi, M. and Takahashi, Y., 2005. Ratchetting of viscoplastic material with cyclic softening, part 1: experiments on modified 9Cr–1Mo steel. *International Journal of Plasticity*, *21*(1), pp.43-65.
42. Yaguchi, M. and Takahashi, Y., 2005. Ratchetting of viscoplastic material with cyclic softening, part 2: application of constitutive models. *International Journal of Plasticity*, *21*(4), pp.835-860.
43. Chaboche, J.L. and Nouailhas, D., 1989. Constitutive modeling of ratchetting effects—part I: experimental facts and properties of the classical models.
44. Sun, L., Liu, L.Q., Wang, R.Z., Wang, X.W., Tan, J.P., Guo, S.J., Wang, J., Zhang, D.W., Zhang, X.C. and Tu, S.T., 2022. A modified damage-coupled viscoplastic constitutive model for capturing the asymmetric behavior of a nickel-based superalloy under wide creep-fatigue loadings. *International Journal of Fatigue*, *164*, p.107160.
45. Zhang, Z., Hu, Z., Schmauder, S., Zhang, B. and Wang, Z., 2019. Low cycle fatigue properties and microstructure of P92 ferritic-martensitic steel at room temperature and 873 K. *Materials Characterization*, *157*, p.109923.
46. Cottrell, A.H., 1956. Dislocations and Plastic Flow in Crystals, Oxford, 1953. *G. Schoeck, Phys. Rev.*, *245*, pp.102-1458.
47. Goyal, S., Veerababu, J., Sandhya, R., Laha, K. and Bhaduri, A.K., 2016. Effect of notch on low cycle fatigue behaviour of 316 LN stainless steel. *Transactions of the Indian Institute of Metals*, *69*(5), pp.1015-1022.

48. Barrett, R.A., Farragher, T.P., O'Dowd, N.P., O'Donoghue, P.E. and Leen, S.B., 2014. Multiaxial cyclic viscoplasticity model for high temperature fatigue of P91 steel. *Materials Science and Technology*, *30*(1), pp.67-74.
49. Norfleet, D.M., Dimiduk, D.M., Polasik, S.J., Uchic, M.D. and Mills, M.J., 2008. Dislocation structures and their relationship to strength in deformed nickel microcrystals. *Acta Materialia*, *56*(13), pp.2988-3001.
50. Lei, X., Li, C., Shi, X., Xu, X. and Wei, Y., 2015. Notch strengthening or weakening governed by transition of shear failure to normal mode fracture. *Scientific reports*, *5*(1), p.10537.

Highlights

- Ratcheting and constraint effects are explored experimentally and theoretically.
- An improved physically based visco-plasticity model is presented, which links the material microstructural features to the cyclic constitutive behaviour.
- The micromechanics origin of the ratcheting was elucidated.
- A mechanism is proposed to explain fatigue notch strengthening in multi-axial LCF tests.
- An additional cyclic softening mechanism was identified under multiaxial LCF conditions.

Declaration of interests

☒ The authors declare that they have no known competing financial interests or personal relationships that could have appeared to influence the work reported in this paper.

☐ The authors declare the following financial interests/personal relationships which may be considered as potential competing interests: